The People's Democratic Republic of Algeria
Ministry of Higher Education and Scientific Research
Dr Yahia Fares University, Medea
Faculty of Technology



Master's Dissertation

In Electrical Engineering

Specialization:

Electrical Control

Automatic and systems

Title

Identification of solar panel parameters using artificial intelligence techniques and the Lambert-W function

Presented by:

DERBALI Karima

KERBOUCI Hadil

Under the guidance and supervision of :

Pr. ABBADI Amel

Pr. HAMIDIA Fethia

Jun 2025

Dedication

I dedicate this modest work:

To the soul of **Lamis Belkhiri**, may God have mercy on her and grant her a place in His vast paradise. We ask God to bless her soul and make her grave a garden among the gardens of Heaven. Her gentle memory will forever remain engraved in my heart.

To my dearest parents, the source of life, love, and affection, for their patience, sacrifices, and unwavering support throughout my journey.

To my brothers and sisters, for their constant presence, encouragement, and to their children, who are true sources of joy and happiness.

To my beloved **Mohamed Amine Meftah**, for his support, love, and invaluable presence in my life.

To all my family members, for their faith in me, their kindness, and their motivation.

And finally, to all the members of the Electrical Engineering family, for the shared moments, the mutual support, and spirit of camaraderie.

Kouki

Dedication

I dedicated this work:

To my parents who have walked beside me, held me up when I stumbled, and never stopped believing in me, even when I doubted myself. Your love has been the foundation of everything I am. Your sacrifices, both seen and unseen have shaped my world and given me the strength to chase my dreams I hope I've made you proud.

To my brothers Thank you for your unwavering support, constant encouragement, and the strength you've given me throughout this journey. Your belief in me has been a guiding light,and I'm truly grateful for everything you've done. This work is a reflection of your love and inspiration.

To my big, wonderful family thank you for being my greatest source of love and support. Each one of you has played a special role in shaping who I am, and this achievement would not have been possible without your prayers, and belief in me. This is for all of you with love and gratitude.

To my dearest friends thank you for being the family I got to choose, your presence during both my brightest and darkest days, and your endless patience and love have carried me through. Each of you brought light into my life in your own unique way, and I am forever grateful.

This work is not mine alone it is a reflection of the love, strength, and support of every person who stood by me. I carry your faith in me in everything I do.
Thank you

Hadil

Acknowledgments

First and foremost, we express our deepest gratitude to Allah for granting us the strength, patience, and determination to complete this work and for guiding us throughout our academic journey.

We would like to extend our heartfelt thanks to our supervisors, **Pr. A. Abbadi** and **Pr. F. Hamidia**, for their constant support, availability, and invaluable guidance. Their expertise, encouragement, and kindness were essential in shaping and enriching this dissertation.

We are sincerely thankful to the jury members, **Dr. Y. Tami** and **Dr. M. A. Khelif**, for graciously accepting to review and evaluate our work, and for dedicating their time and attention to our efforts.

Our gratitude also goes to all the professors of the Electrical Engineering Department, whose knowledge and commitment greatly contributed to our academic development. A special mention goes to **Ms. S. Boukirat** for her continuous moral and practical support throughout our studies.

Lastly, we would like to thank all those who supported us, whether directly or indirectly, throughout this journey. Your time, encouragement, and kindness have been truly appreciated.

ملخص

يتناول هذا العمل تقدير المعلمات الرئيسية في نماذج الخلايا الكهروضوئية باستخدام خوارزميات تحسين متقدمة مستوحاة من الطبيعة، بما في ذلك خوارزمية غزال الجبل (MGO)، وخوارزمية الصقر أحمر الذيل (RTH)، وخوارزمية خنفساء الروث (DBO)، وخوارزمية طائر البفن القطبي (APO). تُطبّق هذه الخوارزميات على كلٍّ من نماذج الخلايا الكهروضوئية أحادية وثنائية الصمام الثنائي، باستخدام بيانات تجريبية من خلايا شمسية سيليكونية تابعة لمركز RTCفرنسا. ولتحسين دقة التقدير وكفاءته، تُستخدم دالة لامبرت-Wكبديل غير تكراري لطريقة نيوتن - رافسون التقليدية. ويُقيّم أداء كلٍّ من هذه الخوارزميات بناءً على جذر متوسط مربع الخطأ (RMSE)وسرعة التقارب. تُظهر النتائج أن خوارزمية RTH، عند دمجها مع دالة لامبرت -W، تُحقق أدقّ تقدير للمُعاملات وأكثرها كفاءة، متفوقةً باستمرار على طريقة نيوتن - رافسون بقيم جذر متوسط مربع أقل وتقارب أسرع. وتُثبت دالة لامبرت-Wميزتها الخاصة من خلال تمكين صياغة واضحة وخالية من التكرار لدالة الهدف، مما يُقلل من التعقيد الحسابي، ويُقلل من وقت التنفيذ، ويُعزز استقرار الحل.

الكلمات المفتاحية: الخلية الكهروضوئية، تقدير المعاملات، خوارزميات التحسين، نيوتن-رافسون، دالة لامبرت -W، نموذج الصمام الثنائي المفرد، نموذج الصمام الثنائي المزدوج، RTCفرنسا، مُحسِّن غزال الجبل(MGO)، خوارزمية الصقر أحمر الذيل(RTH)، مُحسِّن خنفساء الروث (DBO)، مُحسِّن طائر البفن القطبي (APO).

Abstract

This work addresses the estimation of key parameters in photovoltaic (PV) models using advanced nature-inspired optimization algorithms, including the Mountain Gazelle Optimization (MGO) algorithm, Red-Tailed Hawk algorithm (RTH), Dung Beetle Optimization (DBO) algorithm, and Arctic Puffin Optimization (APO) algorithm. These algorithms are applied to both the single-diode and double-diode PV models, using experimental data from RTC France silicon solar cells. To enhance estimation accuracy and efficiency, the Lambert-W function is employed as a non-iterative alternative to the traditional Newton-Raphson method. The performance of each approach is evaluated on the basis of the root mean square error (RMSE) and the convergence speed. The results demonstrate that the RTH algorithm, when combined with the Lambert-W function, achieves the most accurate and efficient parameter estimation, consistently outperforming the Newton-Raphson method with lower RMSE values and faster convergence. The Lambert-W function proves particularly advantageous by allowing for an explicit, iteration-free formulation of the objective function, thereby reducing computational complexity, minimizing execution time, and enhancing solution stability.

Keywords: Photovoltaic cell, Parameter estimation, Optimization algorithms, Newton-Raphson, Lambert function W, Single diode model, Double diode model, RTC France, Mountain Gazelle Optimizer (MGO), Red-tailed Hawk algorithm (RTH), Dung Beetle Optimizer (DBO), Arctic Puffin Optimization (APO).

Résumé

Ce travail porte sur l'estimation des paramètres clés des modèles photovoltaïques (PV) à l'aide d'algorithmes d'optimisation avancés inspirés de la nature, notamment l'algorithme d'optimisation de la gazelle de montagne (MGO), l'algorithme de la buse à queue rousse (RTH), l'algorithme d'optimisation du bousier (DBO) et l'algorithme d'optimisation du macareux moine (APO). Ces algorithmes sont appliqués aux modèles PV à diode unique et à double diode, en utilisant des données expérimentales issues de cellules solaires en silicium RTC France. Pour améliorer la précision et l'efficacité de l'estimation, la fonction Lambert-W est utilisée comme alternative non itérative à la méthode traditionnelle de Newton-Raphson. Les performances de chaque approche sont évaluées en fonction de l'erreur quadratique moyenne (RMSE) et de la vitesse de convergence. Les résultats démontrent que l'algorithme RTH, combiné à la fonction Lambert-W, permet l'estimation des paramètres la plus précise et la plus efficace, surpassant systématiquement la méthode de Newton-Raphson avec des valeurs RMSE plus faibles et une convergence plus rapide. La fonction Lambert-W s'avère particulièrement avantageuse en permettant une formulation explicite et sans itération de la fonction objective, réduisant ainsi la complexité de calcul, minimisant le temps d'exécution et améliorant la stabilité de la solution.

Mots Clée : Cellule photovoltaïque, Estimation des paramètres, Algorithmes d'optimisation, Newton-Raphson, Fonction de Lambert-W, Modèle à une diode, Modèle à double diode, RTC France, Optimiseur de gazelle de montagne (MGO), Algorithme de buse à queue rousse (RTH), Optimiseur de bousier (DBO), Optimisation de macareux moine (APO).

Contents

List of Figures i

List of Tables iv

List of Algorithms v

List of Abriviations and Symbols vi

General Introduction 1

I Photovoltaic System Overview 4

I.1 Introduction . . . 4
I.2 Definition of Photovoltaic . . . 5
I.3 History of Photovoltaic Cells . . . 5
I.4 Solar Radiation . . . 6
I.4.1 Types of Solar Radiation . . . 6
I.5 Photovoltaic Effect . . . 7
I.5.1 PV Cell Power . . . 8
I.5.2 Photovoltaic Cells . . . 8
I.6 Type of Photovoltaic Cell . . . 11
I.6.1 Mono-crystalline Silicon . . . 11
I.6.2 Poly-crystalline Silicon . . . 11
I.6.3 Amorphous Silicon . . . 12
I.6.4 Efficiency . . . 13
I.7 Perovskite Solar Cells . . . 13
I.8 The Parameters of Photovoltaic Cell . . . 14
I.8.1 The Short-Circuit Current I_{sc} . . . 14
I.8.2 The Open-Circuit Voltage V_{oc} . . . 14
I.8.3 The maximum power point P_{mpp} . . . 15
I.8.4 The Fill Factor . . . 15

I.8.5 Efficiency . . . 15
I.9 Electrical Characteristics . . . 15
I.9.1 Current-Voltage Characteristics . . . 15
I.9.2 Power-Voltage Characteristic . . . 16
I.10 Climatic Effect on PV Cell . . . 17
I.10.1 Temperature Influence . . . 17
I.10.2 Irradiance Influence . . . 18
I.11 Photovoltaic Generator . . . 19
I.12 Association of PV Cells . . . 20
I.12.1 Serial Association . . . 20
I.12.2 Parallel Association . . . 21
I.12.3 Series-Parallel Association . . . 22
I.13 Advantages and Disadvantages . . . 22
I.14 Protection of the Photovoltaic System . . . 23
I.15 Conclusion . . . 24

II Metaheuristics Optimization Algorithms 26
II.1 Introduction . . . 26
II.2 Metaheuristics . . . 26
II.2.1 Classification of Metaheuristics . . . 27
II.3 The Mountain Gazelle Optimizer (MGO) . . . 28
II.3.1 The Mathematical Model . . . 29
II.3.2 Mountain Gazelle Optimizer Flowchart . . . 31
II.3.3 Pseudo code of Mountain Gazelle Optimizer . . . 33
II.4 Red-Tailed Hawk Algorithm (RTH) . . . 33
II.4.1 Inspiration and Behavior During Hunting . . . 33
II.4.2 Mathematical Model . . . 34
II.4.3 Pseudo code of Red-Tailed Hawk . . . 38
II.5 Dung Beetle Optimizer (DBO) . . . 38
II.5.1 Inspiration . . . 38
II.5.2 Mathematical Model . . . 39
II.5.3 Dung Beetle Optimization Flowchart . . . 42
II.5.4 Pseudo code Dung Beetle Optimization . . . 43
II.6 Arctic Puffin Optimization (APO) . . . 43
II.6.1 Inspiration . . . 44
II.6.2 Mathematical Model . . . 44
II.6.3 Pseudo code of Arctic Puffin Optimizer . . . 49

II.7 Conclusion 50

III Results and Discussion **51**
III.1 Introduction 51
III.2 Methods for Estimating PV Module Parameters 51
III.2.1 Analytical Methods 52
III.2.2 Iterative Methods 55
III.3 Mathematical Models of Photovoltaic Cell 56
III.3.1 Single-Diode Model (SDM) 56
III.3.2 Double-Diode model (DDM) 57
III.4 RMSE Objective Function 58
III.4.1 For SDM of PV Cell 59
III.4.2 For DDM of PV Cell 59
III.5 Results and Discussion 60
III.5.1 RTC France Silicon Solar Cell Identification 61
III.5.2 Results of Lambert-W function 61
III.5.3 Results of Newton-Raphson method 66
III.5.4 Statistics Analysis 70
III.5.5 Convergence Analysis 71
III.6 Conclusion 73

General Conclusion **74**

Bibliography **76**

A Experimental Data and Measurements **A**

List of Figures

I.1 Types of solar radiation. 7
I.2 Photovoltaic effect. 8
I.3 Photovoltaic cells. 9
I.4 Equivalent circuit of an ideal model PV cell. 9
I.5 Equivalent circuit of Single-Diode model solar cell. 10
I.6 Equivalent circuit of Double-Diode model solar cell. 10
I.7 Mono-crystalline cell. 11
I.8 Poly-crystalline cell. 12
I.9 Amorphous silicon cell. 12
I.10 Current-Voltage characteristic of PV module I=f (V). 16
I.11 Power-Voltage Characteristic of PV module P=f (V). 16
I.12 Current-Voltage characteristics of PV module for different temperatures I(V). 17
I.13 Power-Voltage characteristics of PV module for different temperatures P(V). 18
I.14 Current-Voltage characteristics of PV module for different illuminations I(V). 18
I.15 Power-Voltage characteristics of PV module for different illuminations P(V). 19
I.16 Main composing part of the solar photovoltaic generator. 20
I.17 PV cell in series. 21
I.18 PV cell in parallel. 21
I.19 Series-parallel association of PV cell. 22
I.20 Modules protected by Bypass and Blocking diodes. 24

II.1 Classification of metaheuristic search techniques. 28
II.2 Optimization Procedure of the Mountain Gazelle Optimizer. 31
II.3 Mountain Gazelle Optimizer Flowchart. 32
II.4 Behavior of Red-tailed Hawk during hunting. 34
II.5 Behavior of Red-tailed Hawk during high soaring stage. 35
II.6 Behavior of red-tailed hawk during low soaring stage. 36

II.7 Behavior of red-tailed hawk during stooping and swooping stages. 37
II.8 The rolling dung ball behavior of the dung beetle. 39
II.9 Flowchart of the dung beetle optimization algorithm. 42
II.10 Aerial flight stage of the Arctic puffin. 44

III.1 Equivalent circuit of Single-Diode model solar cell. 56
III.2 Equivalent circuit of Double-Diode model solar cell. 58
III.3 The measured data and estimated data obtained by MGO of single-diode model using Lambert-W function. 62
III.4 The measured data and estimated data obtained by RTH of single-diode model using Lambert-W function. 63
III.5 The measured data and estimated data obtained by DBO of single-diode model using Lambert-W function. 63
III.6 The measured data and estimated data obtained by APO of single-diode model using Lambert-W function. 63
III.7 The measured data and estimated data obtained by MGO of double-diode model using Lambert-W function. 64
III.8 The measured data and estimated data obtained by RTH of double-diode model using Lambert-W function. 65
III.9 The measured data and estimated data obtained by DBO of double-diode model using Lambert-W function. 65
III.10 The measured data and estimated data obtained by APO of double-diode model using Lambert-W function. 65
III.11 The measured data and estimated data obtained by MGO of single-diode model using Newton-Raphson method. 66
III.12 The measured data and estimated data obtained by RTH of single-diode model using Newton-Raphson method 67
III.13 The measured data and estimated data obtained by DBO of single-diode model using Newton-Raphson method. 67
III.14 The measured data and estimated data obtained by APO of single-diode model using Newton-Raphson method. 67
III.15 The measured data and estimated data obtained by MGO of double-diode model using Newton-Raphson method. 68
III.16 The measured data and estimated data obtained by RTH of double-diode model using Newton-Raphson method. 69
III.17 The measured data and estimated data obtained by DBO of double-diode model using Newton-Raphson method. 69

III.18 The measured data and estimated data obtained by APO of double-diode model using Newton-Raphson method. 69
III.19 Convergence curves for SDM and DDM of France silicon solar cell using Lambert-W function. 72
III.20 Convergence curves for SDM and DDM of France silicon solar cell using Newton-Raphson method. 72

List of Tables

I.1 Efficiency of different types of photovoltaic cells. 13

III.1 Upper and lower bound of the SDM, DDM parameters of the RTC FRANCE solar cell. 61
III.2 Optimal parameter values for the SDM model of the RTC France silicon solar cell using Lambert-W function. 62
III.3 Optimal parameter values for the DDM model of the RTC France silicon solar cell using Lambert-W function. 64
III.4 Optimal parameter values for the SDM model of the RTC France silicon solar cell using Newton-Raphson method. 66
III.5 Optimal parameter values for the DDM model of the RTC France silicon solar cell using Newton-Raphson method. 68
III.6 Statistical analysis of SDM using Lambert-W function. 70
III.7 Statistical analysis of DDM using Lambert-W function. 70
III.8 Statistical analysis of SDM using Newton-Raphson method. 71
III.9 Statistical analysis of DDM using Newton-Raphson method. 71

A.1 Measured Current and Voltage Values. . . . . A

List of Algorithms

II.1 Mountain Gazelle Optimization (MGO). 33
II.2 Red-tailed Hawk Optimization (RTH). 38
II.3 Dung Beetle Optimization (DBO). 43
II.4 Arctic Puffin Optimization (APO). 49

List of Abriviations and Symbols

AC	Alternating current
APO	Arctic Puffin Optimization
BMH	Bachelor Male Herds
DBO	Dung Beetle Optimizer
DC	Direct current
DDM	Double-Diode Model
FF	Fill Factor
Levy(dim)	Lévy flight distribution
MGO	Mountain Gazelle Optimizer
MH	Maternity Herds
MSF	Migration to Search for Food
NR	Newton-Raphson Method
PN junction	Positive-Negative junction
PV	Photovoltaic
RMSE	Root Mean Square Error
RMSE_{max}	Maximum RMSE value
RMSE_{min}	Minimum RMSE value
RTH	Red-tailed Hawk Algorithm
SDM	Single-Diode Model

SI	Swarm Intelligence
STD	Standard deviation of the RMSE values
TF	Transition Factor
TSM	Territorial Solitary Males
W-Lambert	Lambert-W Function
cos	The cosine function
D	Diode
$f(X)$, $f'(X)$	Function and its derivative (used in NR method)
G	The illumination (W/m^2)
$G(t)$	Gravity factor
I	Current (A)
I_{L}	The measured current (A)
I_{mpp}	Current at maximum power point (A)
I_{ph}	Photocurrent (A)
I_{sc}	Short-circuit current (A)
I_{sd}, I_{sd1}, I_{sd2}	Diode saturation currents (A)
k	Boltzmann constant
lb	Lower limit of the problem
N	The total number of gazelles
n	Diode ideality factor
n_1, n_2	Additional diode ideality factors
N_p	The number of parallel solar cells
N_s	The number of series cells
P	Power (W)

P_L	The power of the incident light on the cell (W)
P_{mpp}	The maximum power point (W)
q	Electron charge
R	Radius for spiral movement
r_1, r_2	Random values
R_{sh}	Shunt resistance (Ω)
R_{s}	Series resistance (Ω)
s, u, v	Random or constant factors in Lévy equations
T	The temperature measured in Kelvin
t	Current iteration number
$T_{\max}$	Maximum number of iterations
ub	Upper limit of the problem
V	Voltage (V)
V_t	Thermal voltage ($V_t = kT/q$)
V_{L}	The measured voltage (V)
V_{mpp}	Voltage at maximum power point (V)
V_{oc}	Open-circuit voltage (V)
$W(Z)$	Lambert-W function
$X(t)$	Solution at iteration t
X_{best}	Best solution
X_{mean}	Mean of population positions
$\alpha(t)$	Acceleration factor
β	Lévy flight parameter
η	Efficiency

σ	Lévy flight parameter
θ	Angle for spiral movement

General Introduction

The rising global demand for electricity, coupled with growing concerns about environmental degradation and the depletion of fossil fuel resources, has led to increasing interest in sustainable and renewable energy sources [1]. Among these alternatives, solar energy stands out as one of the most promising solutions due to its abundance, cleanliness, and long-term viability. Unlike fossil fuels [2], which are finite and environmentally harmful, solar energy provides a sustainable and eco-friendly alternative that meets future energy needs.

To effectively harness solar energy, photovoltaic (PV) systems have emerged as a reliable and efficient solution. These systems convert sunlight directly into electricity using semiconductor devices known as solar cells. With advancements in PV technology and decreasing production costs [3], PV systems have become widely accessible and economically attractive. They are now deployed extensively in residential, commercial, and industrial sectors. However, ensuring optimal system performance requires accurate modeling of PV cells, which involves estimating key electrical parameters.

PV cell models such as the single-diode and double-diode models [4] include several unknown parameters that describe the electrical behavior of the solar cell. Accurately estimating these parameters is essential for simulating and optimizing PV system performance under various environmental conditions [5].

To overcome this challenge, researchers have increasingly turned to metaheuristic optimization algorithms. These algorithms, inspired by natural phenomena and biological behaviors, offer powerful and flexible strategies for handling complex, high-dimensional, and nonlinear optimization problems. Well-known metaheuristic techniques include evolutionary algorithms (EAs) and swarm intelligence (SI) methods [6]. More recently, several nature-inspired algorithms such as the Mountain Gazelle Optimizer (MGO), Red-Tailed Hawk Algorithm (RTH), Dung Beetle Optimizer (DBO), and Arctic Puffin Optimization (APO) have shown promising results in addressing PV parameter estimation challenges.

In addition to metaheuristic approaches, analytical techniques such as the Lambert-W function are employed to enhance the accuracy and efficiency of parameter estimation in photovoltaic (PV) models. The Lambert-W function is particularly advantageous because it allows for the formulation of an explicit, non-iterative objective function, eliminating the need for complex nested iterations during optimization. This significantly reduces computational complexity, shortens execution time, and ensures faster and more stable convergence. As a result, the use of the Lambert-W function provides a precise and robust alternative to traditional iterative methods, improving the overall performance and reliability of PV system modeling.

This thesis focuses on the application and comparative evaluation of several recent metaheuristic algorithms for estimating the parameters of both single- and double-diode PV model cells. Real experimental data from the RTC France silicon solar cell is used to validate the performance of these algorithms, with simulations implemented in MATLAB. The Newton-Raphson and Lambert-W function methods are also employed to support the parameter estimation process. Algorithm performance is assessed based on metrics such as Root Mean Square Error (RMSE) and convergence speed.

The structure of this work is organized as follows:

Chapter I presents the fundamental concepts of photovoltaic systems. It discusses the photovoltaic effect, the structure and types of solar cells, key performance factors such as irradiance and temperature, as well as the advantages and limitations of solar energy. The purpose of this chapter is to establish a theoretical foundation for understanding PV technologies and to highlight the importance of accurate modeling.

Chapter II This chapter aims to provide an overview of the optimization techniques that will be used for PV parameter estimation. It presents the metaheuristic optimization algorithms: the Mountain Gazelle Optimizer (MGO), Red-Tailed Hawk Algorithm (RTH), Dung Beetle Optimizer (DBO), and Arctic Puffin Optimization (APO). It explains the general principles of these algorithms and the reasons for their selection for this study.

Chapter III details the simulation environment and presents the results obtained using the selected algorithms. It includes a comparative analysis of performance in terms of accuracy and convergence behavior. The objective of this chapter is to evaluate the effectiveness of each algorithm and determine the most suitable ones for solving the PV parameter estimation problem.

Through this study, we aim to contribute to the ongoing research in improving the accuracy and efficiency of PV modeling, ultimately supporting the global shift toward clean and renewable energy systems.

Chapter I

Photovoltaic System Overview

I.1 Introduction

With the growing global demand for electricity and the increasing awareness of environmental sustainability, renewable energy has become a crucial alternative to conventional fossil fuels. Among various renewable sources, solar energy stands out as one of the most promising solutions due to its abundance and sustainability. Unlike fossil fuels such as coal and oil, which are finite and contribute significantly to environmental pollution, solar energy offers a clean, green, and inexhaustible source of power.

Photovoltaic (PV) systems have emerged as an efficient and reliable technology for harnessing solar energy. These systems operate based on the photovoltaic effect, where solar cells convert sunlight directly into electricity [7]. The continuous advancements in PV technology, coupled with the declining cost of solar panels, have made solar energy more accessible and economically viable. While initially favored for remote and off-grid locations, solar power is now being widely integrated into residential, commercial, and industrial applications [8].

This chapter provides an overview of photovoltaic (PV) systems, including their history, how they work, and the types of solar cells used. It explains key performance factors like temperature and irradiance, introduces different PV technologies, and outlines how cells are connected in systems. The chapter also highlights the advantages and limitations of solar energy and emphasizes the need for proper protection to ensure long-term efficiency and sustainability.

I.2 Definition of Photovoltaic

The sun is an inexhaustible, renewable, and free energy source, enabling individuals to generate and consume electricity with confidence through solar power systems. Photovoltaic energy refers to the process of harnessing solar power using solar panels and converting it into electricity through the photovoltaic effect, a phenomenon first discovered by the French physicist Edmond Becquerel in 1839 [9]. This effect occurs when sunlight interacts with certain semiconductor materials, generating an electric current.

The term "photovoltaic," often abbreviated as PV, originates from a combination of "photo," derived from the Greek word for light, and "Volta," named after the Italian physicist Alessandro Volta, who invented the electrochemical battery in 1800. Since its discovery, the photovoltaic effect has been the foundation of solar energy technology, driving significant advancements in renewable energy solutions. Today, photovoltaic systems play a vital role in sustainable energy production, contributing to the global shift toward cleaner and more environmentally friendly power sources.

I.3 History of Photovoltaic Cells

The development of photovoltaic (PV) cells began in the late 1950s, where they were primarily used in satellites for power generation.

In the 1970s, improvements in manufacturing processes and performance led to cost reductions, enabling the use of PV systems in remote terrestrial applications such as telecommunications and battery charging. By the 1980s, PV cells gained popularity in consumer electronics like calculators and watches. Following the global energy crisis, research and investment in PV technologies accelerated, leading to their deployment in residential and commercial settings, including off-grid uses like rural healthcare and water pumping.

In the early 1950s, PV cells were made using silicon wafers, achieving efficiencies of around 6% [10].

In 2010, the average efficiency of commercial silicon-based solar cells stood at about 15%, while today, by 2024–2025, these cells typically operate at around 22%, with some exceeding 25%.Remarkably, Oxford PV has demonstrated that combining perovskite and silicon materials in tandem cells can achieve laboratory efficiencies as high as 28%, signaling promising advancements in next-generation solar technology [11].

I.4 Solar Radiation

Solar radiation refers to the energy emitted by the sun into interplanetary space, a fundamental driver of Earth's climate and energy systems. When discussing the solar energy that reaches the Earth's surface, two key concepts are commonly used: **irradiation** and **irradiance**.

Solar Irradiation: This is the total energy received per unit area over a period of time, measured in joules per square meter (J/m^2). It represents the cumulative solar power received on a surface over a specific duration.

Solar Irradiance: This is the instantaneous power of solar radiation received on a unit area, expressed in watts per square meter (W/m^2). It reflects the intensity of solar energy at a specific moment in time.

Both concepts are critical for designing and analyzing solar energy systems, as they quantify the available solar energy that can be harnessed by photovoltaic systems or solar thermal devices.

I.4.1 Types of Solar Radiation

I.4.1.1 Direct Solar Radiation (Beam Radiation)

Direct radiation is the sunlight that travels in a straight line and reaches the Earth's surface without being scattered by the atmosphere. It is most intense when the sky is clear and is used by concentrating solar power systems (like parabolic troughs and solar towers), which require direct sunlight to focus and generate energy effectively.

I.4.1.2 Diffuse Solar Radiation

This type of radiation is scattered by molecules, dust, and clouds in the atmosphere. It doesn't come directly from the sun's disk but from various parts of the sky. While less intense than direct radiation, diffuse radiation can still be captured by photovoltaic (PV) panels, which can operate on cloudy days due to the scattered light.

I.4.1.3 Reflected Solar Radiation (Albedo Radiation)

Reflected radiation, also known as albedo radiation, is sunlight that is reflected off the ground, bodies of water, buildings, or other surfaces. The amount of reflected radiation

depends on the reflectivity (albedo) of the surface it encounters. For example, snow-covered areas have high albedo and reflect more sunlight than forested or grassy areas.

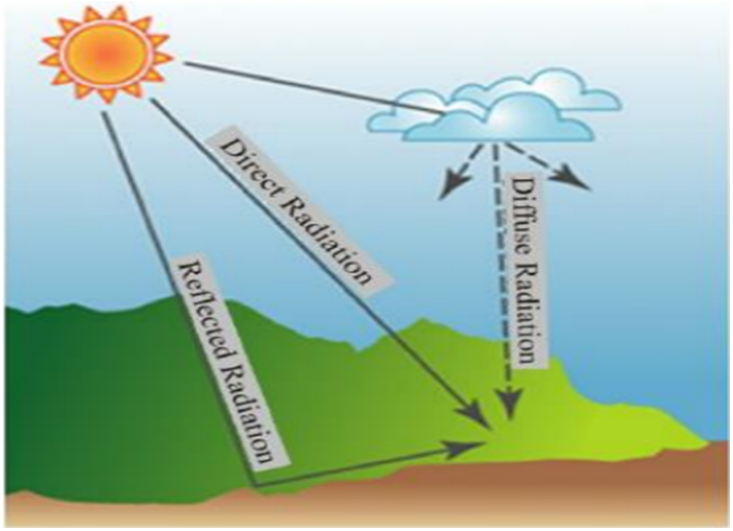


Figure I.1: Types of solar radiation [12].

I.4.1.4 Global Solar Radiation

This is the sum of direct, diffuse, and reflected radiation reaching a horizontal surface on Earth. It is a comprehensive measure of the total solar energy available and is a crucial metric in designing and optimizing solar energy systems.

I.5 Photovoltaic Effect

The photovoltaic effect is the process by which light energy from the sun is directly converted into electricity within solar cells. This occurs when light induces the movement of electrical charges positive and negative within a semiconductor material. The material is typically made up of two layers, separated by a PN junction. One layer is N-doped, containing an excess of electrons, while the other is P-doped, with a deficit of electrons. When these layers are brought together, electrons from the N-doped layer diffuse into the P-doped layer. This movement creates a charge separation, with the N layer becoming positively charged and the P layer becoming negatively charged, facilitating the generation of an electric current.

Figure I.2 illustrates the principle of the PV effect in a PV cell. Essentially, sunlight is composed of photons, which can be considered discrete units of the energy stored in

light. A PV cell is made from semiconductor materials with a p-n junction. When solar radiation strikes a solar cell, some of the photons are absorbed by the cell, resulting in the production of electron-hole pairs. If an external circuit is formed, the voltage difference drives the electrons from the n-side to the p-side of the junction. Consequently, an electric current is formed in the external circuit.

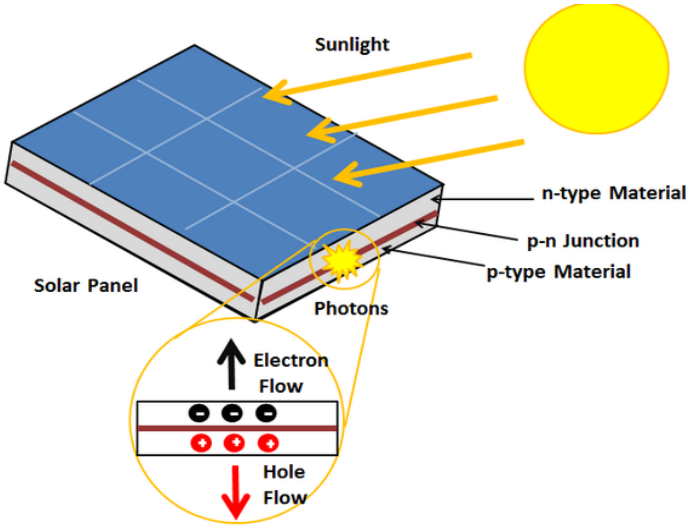


Figure I.2: Photovoltaic effect.

I.5.1 PV Cell Power

Under fixed ambient operating conditions (illuminance, temperature, ambient air circulation speed, etc.), the electrical power P (W) available at the terminals of a PV cell is [13]:

$$P = VI \tag{I.1}$$

P (W): Power supplied by the PV cell.

V (V): Voltage measured across the PV cell.

I (A): Current delivered by the PV cell.

I.5.2 Photovoltaic Cells

Photovoltaic cells are semiconductor devices, typically made from silicon, that convert solar energy directly into electricity. These cells do not require fluids or corrosive materials

and have no moving parts, making them low-maintenance, non-polluting, and silent in operation. As long as they are exposed to sunlight, they continuously generate electricity. This makes photovoltaic cells one of the most environmentally friendly and safe methods of electricity generation [14].

A solar cell operates based on a PN junction, consisting of two layers: a P-layer (positive) and an N-layer (negative). When exposed to sunlight, these cells instantly convert solar radiation into electrical energy. The size of each photovoltaic cell can range from a few square centimeters to 100 cm^2.



Figure I.3: Photovoltaic cells.

I.5.2.1 Ideal Model

The equivalent circuit of an ideal photovoltaic (PV) cell, as shown in Figure I.4 , consists of a current source (I_{ph}) that represents the photocurrent generated by the solar cell. This current source is connected in parallel with a diode, which models the behavior of the PN junction and determines the voltage across the cell. Various models of solar cells exist, each representing different aspects of the cell's performance.

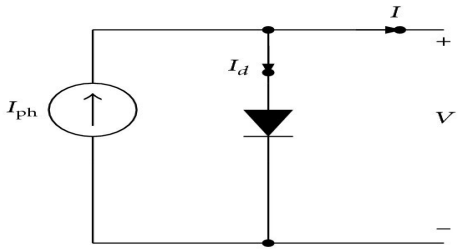


Figure I.4: Equivalent circuit of an ideal model PV cell.

I.5.2.2 Practical One-Diode Model

Figure I.5 illustrates the equivalent circuit of a real solar cell, which incorporates parasitic resistive effects due to the manufacturing process. This diagram includes a shunt resistor (R_{sh}), which models the leakage current between the top grid and the rear contact, typically larger than the series resistor (R_{s}). A diode (D) represents the PN junction, while a current source (I_{ph}) models the photocurrent generated by the cell. Additionally, the series resistor (R_{s}) accounts for the Joule heating losses within the cell.

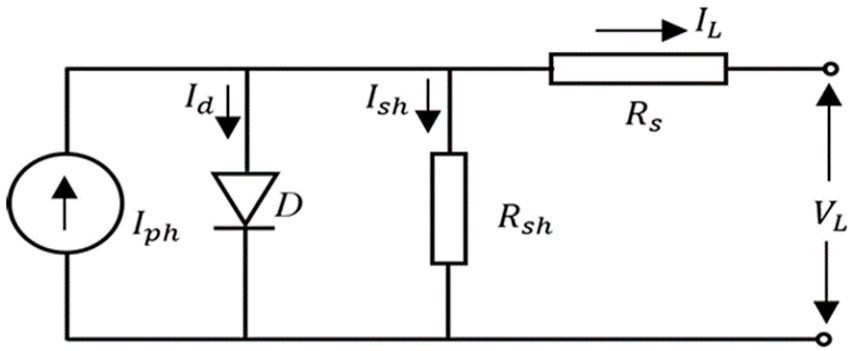


Figure I.5: Equivalent circuit of Single-Diode model solar cell [15].

I.5.2.3 Practical Two-Diode Model

The model is represented by the equivalent electrical diagram shown in Figure I.6 . In this model, a current source simulates the luminous flux, while two resistors, the shunt resistor (R_{sh}) and series resistor (R_{s}), represent the parasitic resistive effects. Additionally, two diodes account for the cell's polarization and the losses due to minority carrier recombination.

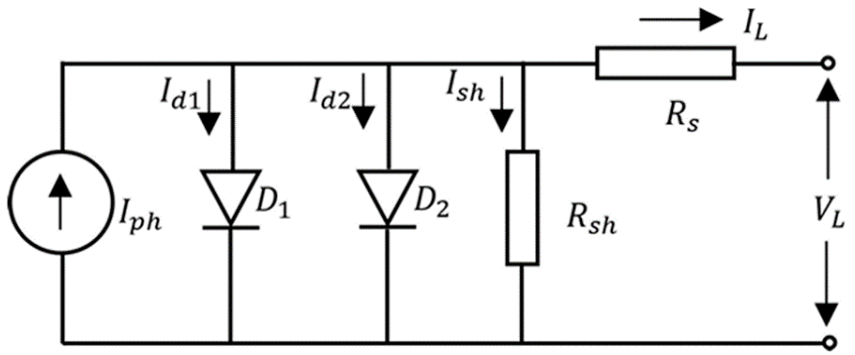


Figure I.6: Equivalent circuit of Double-Diode model solar cell [15].

I.6 Type of Photovoltaic Cell

There are different types of PV cells and different generations, they are made from semiconductor materials (mono-crystalline silicon, poly-crystalline silicon, amorphous silicon).

The efficiency of a semiconductor material is of great importance because, on an equal surface, it can be of different interest from one material to another. There are many, but silicon, present in large quantities on the Earth's surface, is the second most abundant element after oxygen and is the most widely used [16].

I.6.1 Mono-crystalline Silicon

Mono-crystalline silicon, also called single-crystal Silicon, is the result of molten silicon cooling. Once solidified, it becomes a uniform crystal that is cut into thin slices to form the photovoltaic cell. Mono-crystalline cells are recognized by their very dark blue color, without any trace of crystals or other features [17].



Figure I.7: Mono-crystalline cell.

I.6.2 Poly-crystalline Silicon

Globally, in the world, it is the most used type of photovoltaic cell, because it offers the best price/quality until now compared with mono-crystalline silicon. These cells are composed of crystals oriented in different directions. To obtain poly-crystalline silicon, also known as Multi-crystalline, the silicon is melted in a square metal mold. The color of this type of cell is blue and dotted with patterns left by the crystals. This feature allows us to recognize this photovoltaic cell easily [17].

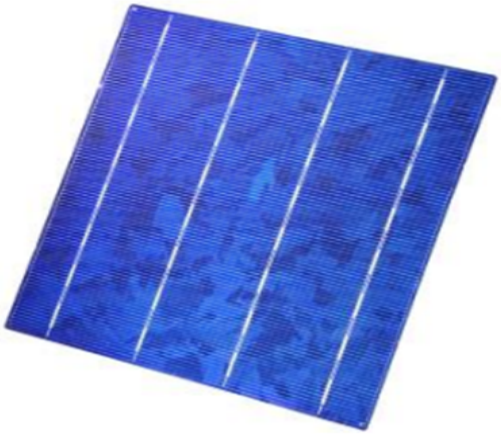


Figure I.8: Poly-crystalline cell.

I.6.3 Amorphous Silicon

They are the cheapest photovoltaic cells to make. They are much finer than mono-crystalline or crystalline polys. It is mainly used for low-power equipment.

Amorphous silicon is obtained from silicon gas. This gas is vaporized on a support, made of glass, flexible plastic, or metal, using a vacuum spraying process. These photovoltaic cells are dark gray [16].

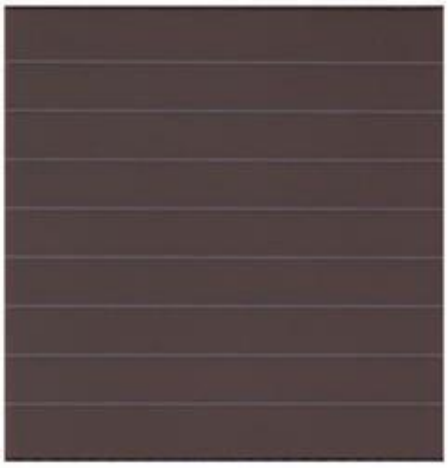


Figure I.9: Amorphous silicon cell.

I.6.4 Efficiency

Tableau I.1: Efficiency of different types of photovoltaic cells [18].

Cell type	Efficiency	Lifetime	Characteristics
Mono-crystalline Silicon	17–22%	20 to 30 years	• Very good performance. • High cost. • Low efficiency under reduced illumination.
Poly-crystalline Silicon	16–18%	20 to 30 years	• Good performance/price ratio. • Low efficiency under reduced illumination.
Amorphous Silicon	6–11%	(±10 years)	• Operates under low illumination. • Low manufacturing cost.

I.7 Perovskite Solar Cells

Perovskite solar cells have a higher energy conversion efficiency than other types of solar cells. They have achieved efficiencies of more than 20 to 25 percent in laboratory settings. Perovskite solar cells have several advantages, including high absorption, good energy conversion efficiency, long carrier lifetime, tunable bandgap width, and relatively low manufacturing cost. These features make them an interesting emerging photovoltaic technology.

While perovskite solar cells have potential in terms of efficiency, silicon solar cells are currently more stable and mature for commercial applications. The disadvantage of perovskite cells is their instability and low resistance to external agents like water and temperature. However, promising research is currently underway, which should make this type of cell more attractive [19].

One area of particular interest in photovoltaic research is combining perovskite with another technology, typically silicon, to improve cell efficiency. A cell that combines perovskite with silicon can achieve higher efficiency over a wider range of wavelengths. In June 2018, these tandem cells achieved an efficiency of 25.2% for a perovskite-silicon cell. In the future, as technology improves, perovskite solar cells may make greater breakthroughs in energy efficiency [20].

I.8 The Parameters of Photovoltaic Cell

The performance of a photovoltaic cell is characterized by a certain number of key parameters. The value of these parameters varies more or less according to a certain number of external parameters, including the cell lighting level and temperature.

I.8.1 The Short-Circuit Current I_{sc}

This value represents the current generated by an illuminated cell when it is short-circuited (connected to itself). This is the highest value of the current generated by a cell. It is produced under short-circuit conditions: V = 0 [21]. In the case of the Single Diode Model, the short-circuit current is obtained by applying equation I.2.

In the ideal case ($R_s = 0$, $R_{sh} = \infty$)

$$I_{sc} = I_{ph} - I_{sd}\left(-1 + e^{\left(\frac{V_{oc}+R_s I_{sc}}{n \cdot V_t}\right)}\right) - \frac{V_{oc} + R_s I_{sc}}{R_{sh}} \tag{I.2}$$

For most cells (with low series resistance), the terms:

$$I_{sd}\left(-1 + e^{\left(\frac{V_{oc}+R_s I_{sc}}{n \cdot V_t}\right)}\right); and \frac{V_{oc} + R_s I_{sc}}{R_{sh}} \tag{I.3}$$

can be neglected

The approximate expression for the short-circuit current is:

$$I_{\mathrm{sc}} = I_{\mathrm{ph}} \tag{I.4}$$

I.8.2 The Open-Circuit Voltage $V_{\mathbf{oc}}$

The open-circuit voltage is the maximum voltage generated by the photovoltaic cell. It represents the voltage measured at the terminals of the cell under illumination without a load circuit when the current flowing through the cell is zero.

It can be calculated from the relationship as follows [21].

$$0 = I_{\mathrm{ph}} - I_{sd}\left(-1 + e^{\left(\frac{V_{\mathrm{oc}}}{n \cdot V_t}\right)}\right) - \frac{V_{\mathrm{oc}}}{R_{\mathrm{sh}}} \tag{I.5}$$

In the ideal case, the value of V_{oc} is

$$V_{\mathrm{oc}} = n \cdot V_t \ln\left(1 + \frac{I_{\mathrm{ph}}}{I_{sd}}\right) \tag{I.6}$$

With $V_t = \frac{kT}{q}$ is known as thermal voltage .

I.8.3 The maximum power point $P_{\mathbf{mpp}}$

This is the relationship between the maximum voltage V_{mpp} and maximum current I_{mpp} under standard sunshine conditions (temperature = 25°C and illuminance = 1000 W/m^2) [22].It is given by the relationship

$$P_{\text{mpp}} = V_{\text{mpp}} \cdot I_{\text{mpp}} \tag{I.7}$$

I.8.4 The Fill Factor

The fill factor is an important metric used to evaluate the performance and electrical characteristics of a photovoltaic cell. It is defined as the ratio between the maximum power and the product of the cell's short-circuit current I_{sc} and open-circuit voltage V_{oc} [9], which can be expressed as follows:

$$FF = \frac{P_{\text{mpp}}}{I_{\text{sc}} V_{\text{oc}}} = \frac{I_{\text{mpp}} V_{\text{mpp}}}{I_{\text{sc}} V_{\text{oc}}} \tag{I.8}$$

I.8.5 Efficiency

Efficiency is defined as the ratio between the maximum power produced by the cell, P_{mpp}, and the power of the incident light on the cell, P_L [9].

$$\eta = \frac{P_{\text{mpp}}}{P_L} \tag{I.9}$$

I.9 Electrical Characteristics

I.9.1 Current-Voltage Characteristics

The photovoltaic cell has a non-linear (I-V) characteristic; the electrical power delivered by a photovoltaic cell is the product of the voltage by the current it generates. These two quantities, current and voltage, depend at the same time on the electrical properties of the cell but also on the electric charge at its terminals. They are synthesized in a graph called the characteristic current-voltage.

At a fixed temperature and illumination, the current-voltage characteristic of a cell looks like the following:

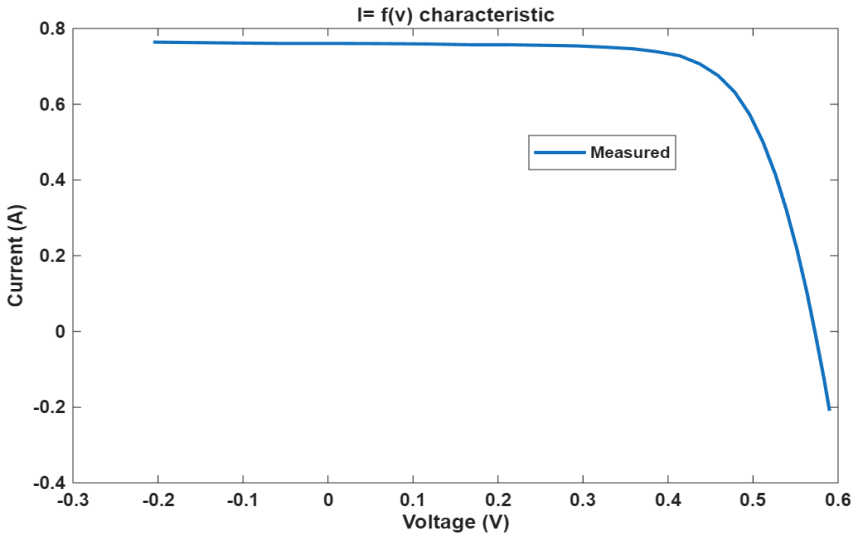


Figure I.10: Current-Voltage characteristic of PV module I=f (V).

I.9.2 Power-Voltage Characteristic

To determine the power output of a solar cell, one can simply multiply the current (I) flowing through it by the voltage (V) across it. This results in the expression for power (P), which is represented by the formula: ($P = VI$)

By applying this formula and mapping the resulting values of P against V on a graph, a clear representation of the relationship between the two can be obtained. In this diagram, ($P = f(V)$).

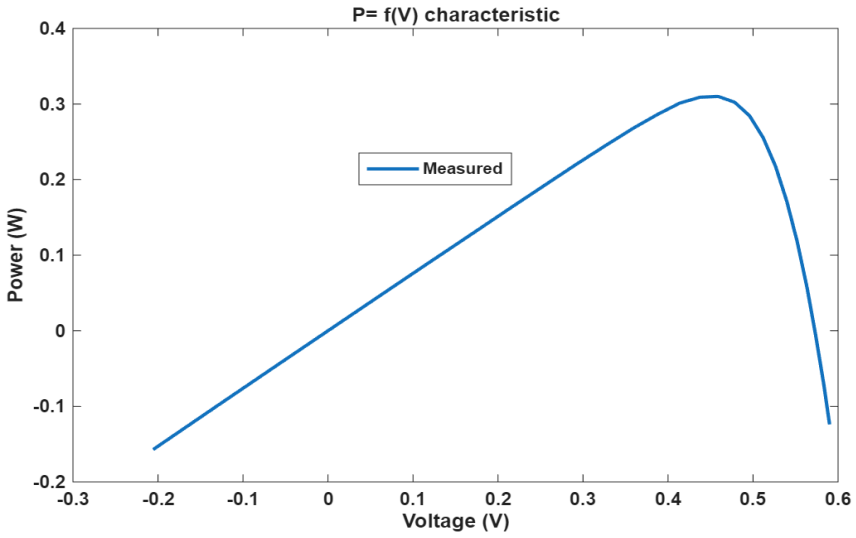


Figure I.11: Power-Voltage Characteristic of PV module P=f (V).

I.10 Climatic Effect on PV Cell

Temperature and irradiance significantly affect the performance and characteristics of photovoltaic cells, also referred to as PV generators. Both factors influence how efficiently these cells convert sunlight into electricity, with higher temperatures often leading to decreased efficiency and increased irradiance enhancing performance.

I.10.1 Temperature Influence

Temperature is an important parameter in the behavior of photovoltaic cells. Figure I.12 shows the current-voltage $I(V)$ characteristics for different temperatures ($T = 0°C,\ 25°C,\ 50°C,\ 75°C$). Here, the illumination is fixed at ($G = 1000\ \mathrm{W/m^2}$).

The open-circuit voltage decreases with increasing temperature, while the short-circuit current increases slightly with increasing temperature. Therefore, the influence of temperature on I_{sc} can be neglected in most cases.

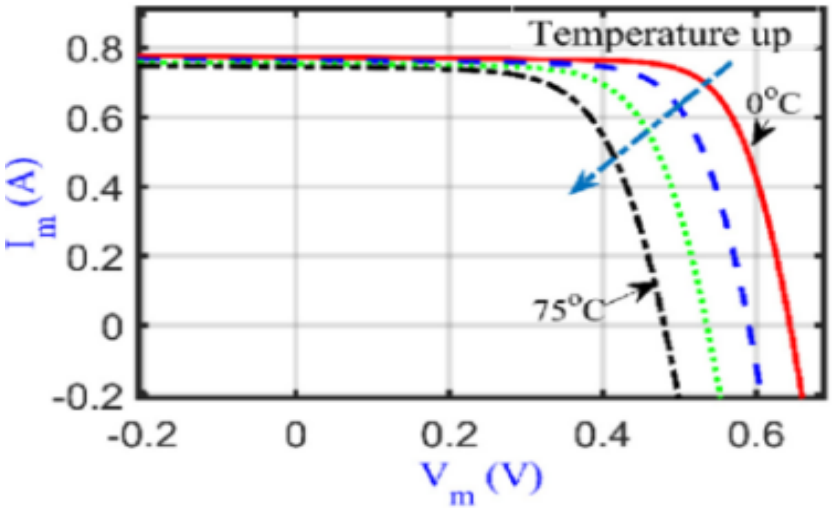


Figure I.12: Current-Voltage characteristics of PV module for different temperatures I(V) [23].

In Figure I.13, the maximum power decreases as open-circuit voltage decreases due to an increase in temperature. It can be concluded that temperature has a negative influence on open-circuit voltage.

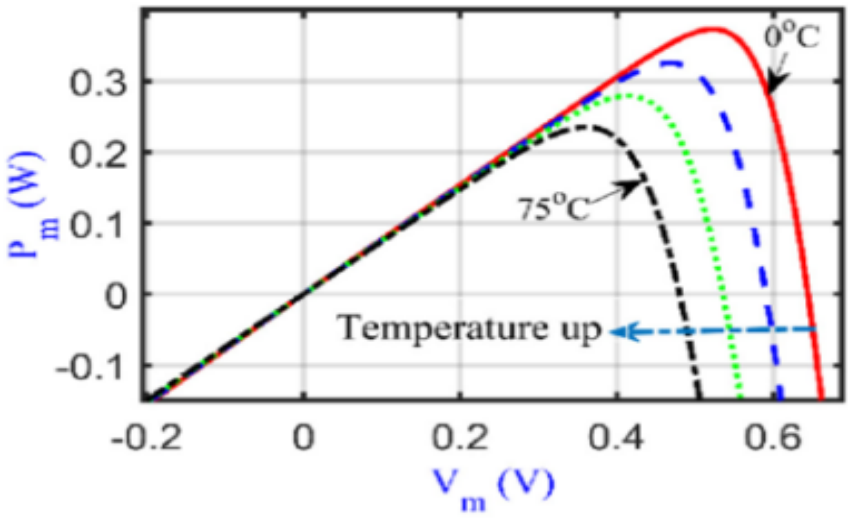


Figure I.13: Power-Voltage characteristics of PV module for different temperatures P(V) [23].

I.10.2 Irradiance Influence

The main source of energy for photovoltaic (PV) modules is radiation from the sun. The amount of solar radiation that a PV module receives depends on various factors such as the module's angle and orientation, the location's latitude and longitude, and the time of day and year.

Figures I.14 and I.15 show the influence of different illuminances on the current-voltage ($I = f(V)$) and power-voltage ($P = f(V)$) characteristics at a constant temperature ($T = 25°C$).

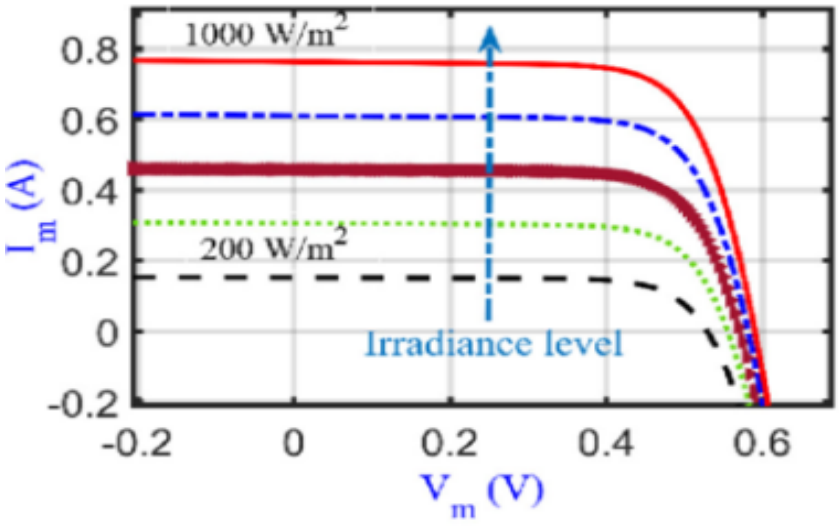


Figure I.14: Current-Voltage characteristics of PV module for different illuminations I(V) [23].

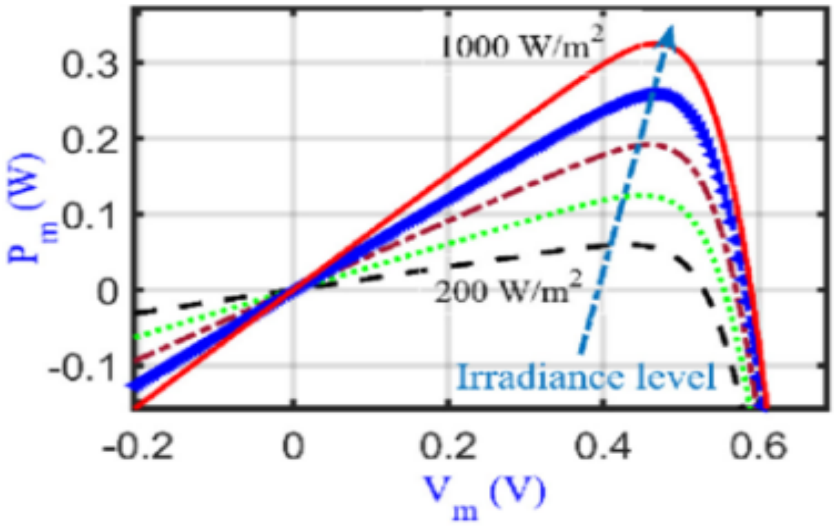


Figure I.15: Power-Voltage characteristics of PV module for different illuminations P(V) [23].

The increase in irradiance causes an increase in the maximum power as the current increases significantly, but the voltage changes very little. Because the photocurrent is directly proportional to the irradiance level, while the open-circuit voltage is a logarithmic function and is usually ignored.

Temperature and irradiance are therefore the two main parameters that will change the characteristics of a PV generator. These two parameters should therefore be carefully considered in the sizing of a PV installation.

I.11 Photovoltaic Generator

A photovoltaic module is an electrical generator that converts the energy from sunlight photons into electricity through the photoelectric effect. This module is made up of multiple photovoltaic cells, which are connected electrically to form a complete unit. Several modules are then connected together to create a photovoltaic array, which can be arranged either in series, parallel, or a combination of both, depending on the desired electrical output.

The assembly of these modules provides several benefits:

It ensures the generation of sufficient voltage.

It protects the cells and their metal contacts from external environmental factors, such as humidity.

It offers mechanical protection to the cells, safeguarding them from physical damage like shocks.

In a photovoltaic generator, the modules are arranged to achieve the desired electrical characteristics, such as power output, short-circuit current, and open-circuit voltage. The direct current (DC) produced by the generator is then often converted into alternating current (AC) using an inverter for various applications.

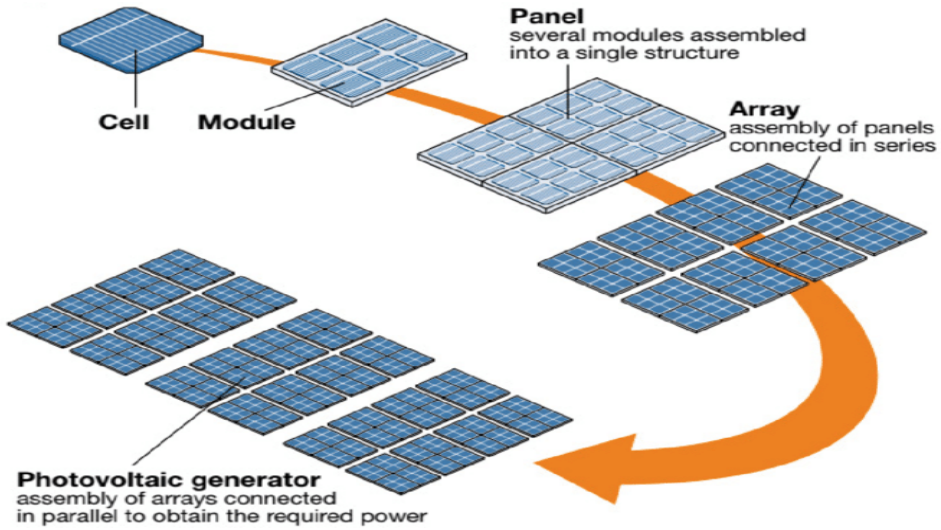


Figure I.16: Main composing part of the solar photovoltaic generator.

I.12 Association of PV Cells

I.12.1 Serial Association

A combination of N_s cells in series increases the voltage of the photovoltaic module. The cells are then crossed by the same current and the characteristic resulting from the serial grouping is obtained by adding the elementary voltages of each cell. The equation summarizes the electrical characteristics of a series of N_s cells [24].

$$V'_{\text{oc}} = N_s V_{\text{oc}} \tag{I.10}$$

V_{oc}: open-circuit voltage

N_s: number of series-connected cells

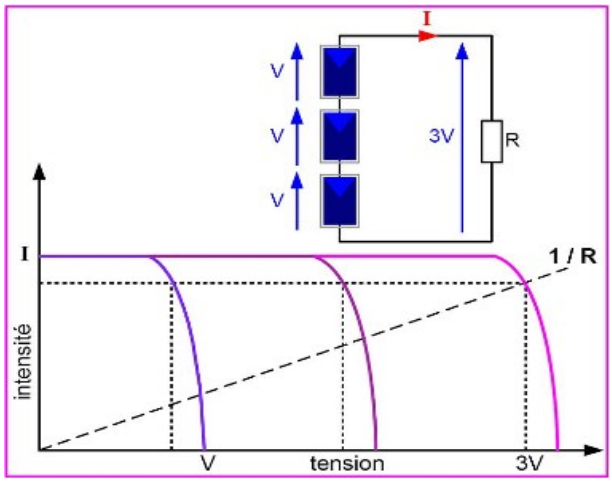


Figure I.17: PV cell in series.

I.12.2 Parallel Association

A parallel association of N_p cells is possible and allows for an increase in the output current of the module, thus created. In a group of identical cells connected in parallel, the cells are subjected to the same voltage, and the characteristic resulting from the group is obtained by the addition of currents. The equation, in turn, summarizes the electrical characteristics of a parallel association of N_p cells.

$$I'_{\text{sc}} = N_p I_{\text{sc}} \tag{I.11}$$

I_{sc}: short-circuit current

N_p: number of parallel-connected cells

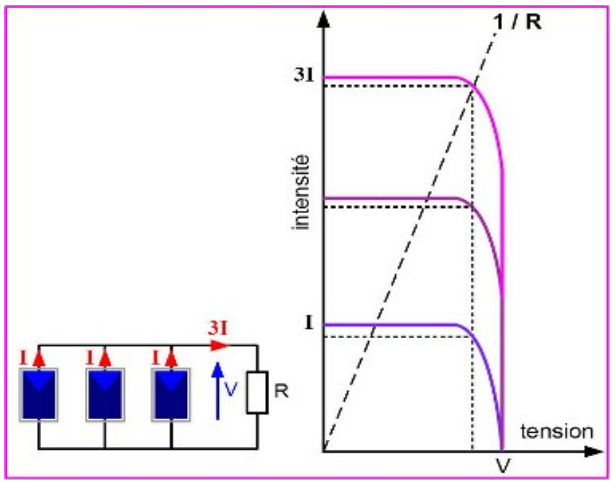


Figure I.18: PV cell in parallel.

I.12.3 Series-Parallel Association

Connecting several cells in series forms a cell string, which increases the voltage for the same current while assembling several cell strings in parallel forms a module, which increases current and maintains voltage. An association of several modules in the same plane is called a panel, and the assembly of several panels in rows of series and parallel panels forms a photovoltaic field [24].

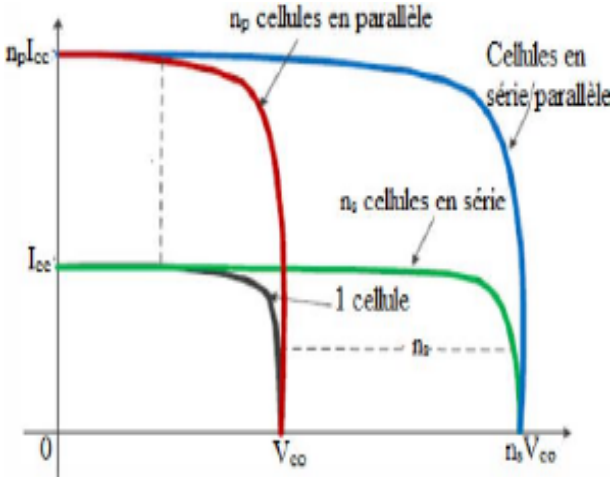


Figure I.19: Series-parallel association of PV cell.

Note:

To function optimally, a PV module is important to select the most identical cells possible when making a module, that is, the cells series-parallel (N_s,N_p) all behave in the same way. They must come from the same technology, the same operating conditions (illumination, temperature, ageing, and inclination).

I.13 Advantages and Disadvantages

Main Advantages of Photovoltaic Energy

Clean and Eco-friendly: It is non-polluting, produces no greenhouse gases, and generates no waste.

Low Maintenance: Photovoltaic systems use reliable, long-lasting components that require minimal maintenance.

Low Operating Costs: Operational expenses are very low, mainly due to minimal maintenance and the need for a small, less specialized workforce.

Main Disadvantages of Photovoltaic Energy

High Initial Investment: The production of photovoltaic panels requires advanced technology and significant investment in research, development, and manufacturing equipment.

Intermittency: Photovoltaic energy generation is dependent on sunlight, making it an unstable and unpredictable source of electricity.

Limited Lifespan: Photovoltaic installations typically last 20 to 30 years, and their efficiency tends to decrease over time and under varying operating conditions.

I.14 Protection of the Photovoltaic System

The protection of PV systems is important to ensure the continuity in service, increase their lifespan, in particular by avoiding destructive breakdowns related to the association of cells, their functions, and protect PV panels against lightning.

Solar panels are often subjected to environmental conditions, such as temperature variations, humidity, strong winds, bad weather, and the risk of vandalism or theft.

When installing solar panels, it is important to ensure that they are able to withstand extreme weather conditions such as high winds. Additionally, a secure fastening system should be put in place to prevent the panels from becoming detached or falling off, which could cause damage to property or individuals. Electrical connections should also be protected using waterproof connectors and suitable cables to prevent short circuits or damage caused by moisture. Lightning and overvoltage protection devices should be utilized to prevent damage from electrical discharges. Furthermore, security measures should be taken to prevent vandalism or theft, such as installing security fencing, surveillance cameras, or alarms. Effective protection measures ensure the safety of people and property while also ensuring reliable and stable energy production over the long term.

The main enemy of PV systems is darkness, whether it is shadow or nighttime. The key to both of these impacts

Hot-spot phenomenon: is a phenomenon that occurs when a shadow falls on one of the photovoltaic panel's cells or on part of it (the main cause is the shading effect).

Shading in one part of the module causes it to function as a receiver, so the current of the string comes to this panel, which results in an explosion or a combustion of this panel. The ideal solution to eliminate this phenomenon is a bypass diode [24].

Overnight, to avoid battery discharge in the reverse direction is important to place a blocking diode, blocking diode prevents current from flowing in the reverse direction. It is an essential component in solar panels that stops your solar array from discharging at night or when the batteries are full. Blocking diodes are also known as 'rectifiers' because they allow current to flow in one direction and prevent the reverse flow.

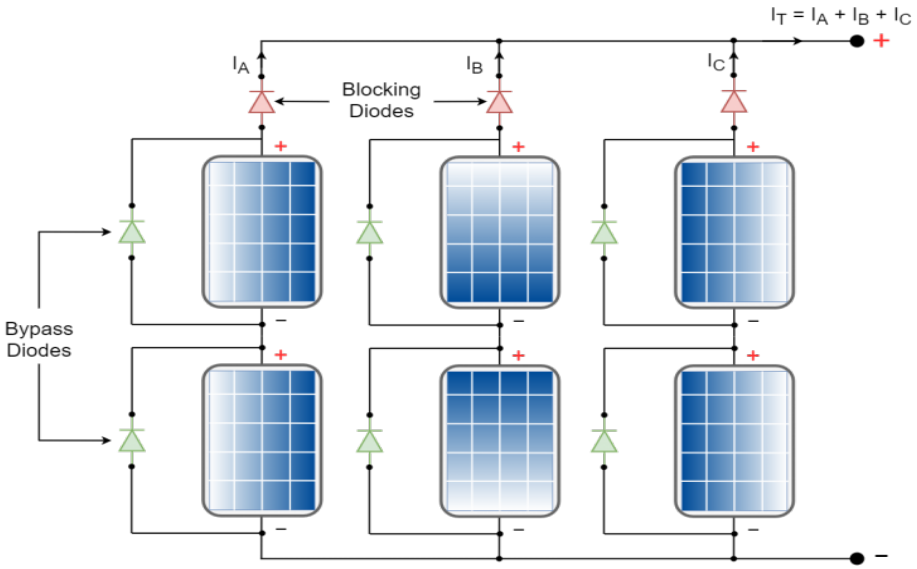


Figure I.20: Modules protected by Bypass and Blocking diodes.

I.15 Conclusion

In this chapter, we provided an overview of photovoltaic solar energy, covering the key components of a photovoltaic system. We explored the photovoltaic effect, the structure of PV cells, and the various parameters that influence their performance. The chapter also discussed different types of photovoltaic technologies and highlighted their advantages and disadvantages.

We examined how essential it is to model a photovoltaic panel based on weather conditions, such as sunlight exposure, to maximize power output. This modeling process is a crucial step in evaluating the performance characteristics of solar panels, ensuring their efficiency under varying environmental factors.

Chapter II

Metaheuristics Optimization Algorithms

II.1 Introduction

Metaheuristic optimization algorithms have emerged as powerful tools for tackling complex and nonlinear optimization problems where conventional techniques often fall short. These algorithms, inspired by natural, biological, and physical processes, offer flexible frameworks that balance exploration and exploitation in diverse problem spaces. This chapter presents a detailed overview of metaheuristics algorithms, focusing specifically on four recently developed and nature-inspired approaches: Mountain Gazelle Optimizer (MGO), Red-tailed Hawk Algorithm (RTH), Dung Beetle Optimizer (DBO) and Arctic Puffin Optimization (APO).

These algorithms were selected for their novelty, biological diversity of inspiration, effectiveness in escaping local optima, and promising performance in handling multimodal, high-dimensional, and constrained optimization problems. By analyzing and comparing their strategies, this chapter aims to highlight how nature-inspired intelligence can be leveraged for efficient and reliable optimization in engineering and computational science.

II.2 Metaheuristics

Metaheuristics are optimization algorithms used to solve complex, nonlinear problems without necessarily finding the global optimum. Unlike traditional methods, they do not rely on derivatives or equation simplification, but instead use intelligent search strategies. These algorithms are widely applied in fields like engineering, management,

healthcare, and planning due to their ability to handle problems with multiple constraints and conflicting objectives. Their strength lies in thoroughly exploring the search space, increasing the chances of finding effective solutions.

Various types of metaheuristics have emerged, including nature-inspired, physics-based, and stochastic algorithms. Many are population-based, maintaining and improving a set of potential solutions over time. The goal is to make the best use of limited resources and time to solve real-world, complex optimization problems [25].

II.2.1 Classification of Metaheuristics

Metaheuristic algorithms can be classified in several ways based on different criteria. Here are some common classifications:

II.2.1.1 Nature-inspired vs Non Nature-inspired

Metaheuristics are classified based on their inspiration by natural processes or not Nature-inspired metaheuristics include genetic algorithms, particle swarm optimization, and ant colony optimization. Non nature-inspired metaheuristics include simulated annealing and tabu search.

II.2.1.2 Deterministic vs Stochastic

Deterministic metaheuristics produce and assess candidate solutions using a deterministic process that usually involves methodical solution space search. Hill climbing and tabu searching are two examples. Randomness is introduced into the search process via stochastic metaheuristics, which frequently employ probabilistic techniques for the generation, evaluation, or selection of solutions. Genetic algorithms and simulated annealing are two such examples.

II.2.1.3 Trajectory-based vs Population-based

Metaheuristics can be classified based on whether they aim to identify a single or several solutions. Trajectory-based metaheuristics aim to find a single solution and refine it iteratively. Examples include hill climbing and simulated annealing. Population-based metaheuristics utilize a set of solutions to explore the search space. Examples include genetic algorithms and particle swarm optimization.

II.2.1.4 Local Search-based vs Global Search-based

Local search metaheuristics aim to improve a single solution by making incremental modifications to it, focusing on the nearby neighborhood of the current solution. Examples include hill climbing and gradient descent.

Global search metaheuristics, on the other hand, explore a broader area of the solution space in search of a global optimum. These techniques often sacrifice efficiency to avoid being trapped in local optima. Examples include genetic algorithms and simulated annealing [26].

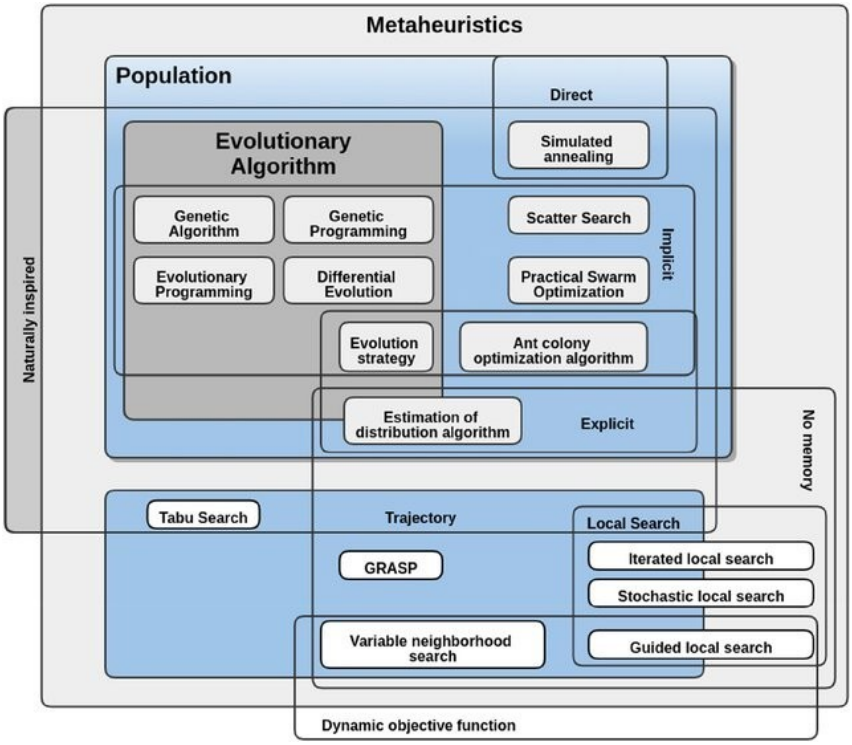


Figure II.1: Classification of metaheuristic search techniques [26].

II.3 The Mountain Gazelle Optimizer (MGO)

The Mountain Gazelle Optimizer (MGO) is inspired by the social behavior and life patterns of mountain gazelles. It incorporates four key behavioral aspects: bachelor male herds, maternity herds, solitary territorial males, and migration in search of food. Each gazelle (X_i) is assigned to one of these groups, and new solutions (gazelles) can emerge from any of them. In MGO, the best global solution is represented by adult males in territorial herds. One-third of the population, consisting of young bachelor males with higher cost values, lacks the maturity to lead or reproduce. Maternity herds contain

strong gazelles that effectively balance exploration and exploitation by moving toward optimal solutions while also investigating new areas of the search space.

At the end of each iteration, strong gazelles (effective solutions) are retained, while weak ones with higher costs are eliminated from the population [27].

II.3.1 The Mathematical Model

II.3.1.1 Territorial Solitary Males (TSM)

When male mountain gazelles mature and attain strength, they establish individual territories and display territorial behavior, with substantial spaces between territories. The conflict between adult male gazelles occurs over territory control or mating rights to the females.Young males attempt to take over the territory or female, while adult males strive to defend their territory. Eq II.1 to Eq II.3 have been utilized to simulate the adult male's territory.

$$TSM = male_{gazelle} - |(ri_1 \times BH - ri_2 \times X(t)) \times F| \times cof_r \tag{II.1}$$

$$\mathrm{BH} = X_{ra} \times |r_1| + M_{pr} \times |r_2| \quad \Rightarrow \quad r_a = \left\{ \left(\frac{N}{3} \ldots N \right) \right\} \tag{II.2}$$

$$F = N_1(D) \times \exp\left(2 - \mathrm{t} \times \left(\frac{2}{T_{max}}\right)\right) \tag{II.3}$$

In Eq II.1, the $male_{gazelle}$ represents the position vector of the globally optimal solution (adult male). The variables ri_1 and ri_2 are random integers 1 or 2. BH is the coefficient vector associated with the group of young males, computed using Eq II.2. The factor F is calculated using Eq II.3. cof_r is a randomly chosen coefficient vector that is updated in each iteration to enhance the search capability, and it is computed using Eq II.4.

In Eq II.2, X_{ra} refers to a randomly selected solution (young male) within the range defined by r_a. M_{pr} represents the average number of randomly selected search agents. N denotes the total number of gazelles, and r_1 and r_2 are random values in the range $[0, 1]$.

In Eq II.3, N_1 is a random number derived from a standard distribution matching the dimensionality of the problem. The exponential function is denoted by exp. T_{max} indicates the maximum number of iterations, and t refers to the current iteration number [27].

$$Cof_i = \begin{cases} (a+1) + r_3, \\ a \times N_2(D), \\ r_4(D), \\ N_3(D) \times N_4(D)^2 \times \cos\left((r_4 \times 2) \times N_3(D)\right) \end{cases} \tag{II.4}$$

$$a = -1 + t \times \left(\frac{-1}{T_{max}}\right) \tag{II.5}$$

In Eq II.4, a is a calculated using Eq II.5, while r_3 and r_4 are random numbers within the range of 0 and 1. N_1, N_2, N_3 and N_4 are random numbers in the standard range and dimensions of the problem. In the problem dimensions, r_4 is also a random number between 0 and 1. Finally, **cos** represents the Cosine function [27].

II.3.1.2 Maternity Herds (MH)

Maternity herds play a vital role in the life cycle of mountain gazelles, as they are responsible for giving birth to strong male offspring. Male gazelles may also take part in the birthing process, and young males often attempt to compete for the attention of females, which is modeled using Eq II.6.

$$\mathrm{MH} = \left(\mathrm{BH} + \mathrm{cof}_{1,r}\right) + \left(ri_3 \times \mathrm{male}_{\mathrm{gazelle}} - ri_4 \times X_{\mathrm{rand}}\right) \times \mathrm{cof}_{1,r} \tag{II.6}$$

In Eq II.6, BH represents the impact factor vector of the young, calculated using Eq II.2 . The $male_{gazelle}$ stands for the best global solution (adult male) in the current iteration. Finally, X_{rand} is the vector position of a randomly selected gazelle from the entire population [27].

II.3.1.3 Bachelor Male Herds (BMH)

As male gazelles grow stronger, they establish their own territory and compete to control female gazelles. Young males fight against adult males for the territory and possession of the females, sometimes resulting in violent confrontations.

$$\mathrm{BMH} = \left(X(t) - D\right)\left(ri_5 \times \mathrm{male}_{\mathrm{gazelle}} - ri_6 \times \mathrm{BH}\right) \times \mathrm{cof}_r \tag{II.7}$$

$$D = \left(|X(t)| + |\mathrm{male}_{\mathrm{gazelle}}|\right) \times \left(2 \times r_6 - 1\right) \tag{II.8}$$

This behavior is represented mathematically in Eq II.7 using variables such as $X(t)$ (the position of the gazelle in the current iteration), D (calculated using Eq II.8), ri_5 and ri_6 (random integers 1 or 2), BH (the impact factor of the young male herd, calculated using Eq II.2), $\text{male}_{\text{gazelle}}$ (the position of the male gazelle, the best solution), and r_6 (a random number between 0 and 1). Eq II.8 uses $X(t)$ and $\text{male}_{\text{gazelle}}$ (positions of the gazelle vectors in the current iteration and the best solution, respectively) [27].

II.3.1.4 Migration to Search for Food (MSF)

Mountain gazelles roam to find food and migrate due to their high speed and jumping ability. The behavior is modeled in Eq II.9 as follows:

$$\text{MSF} = (ub - lb) \times r_7 + lb \tag{II.9}$$

Where ub and lb represent the upper and lower limits of the problem, respectively, and r_7 is a random number between 0 and 1.

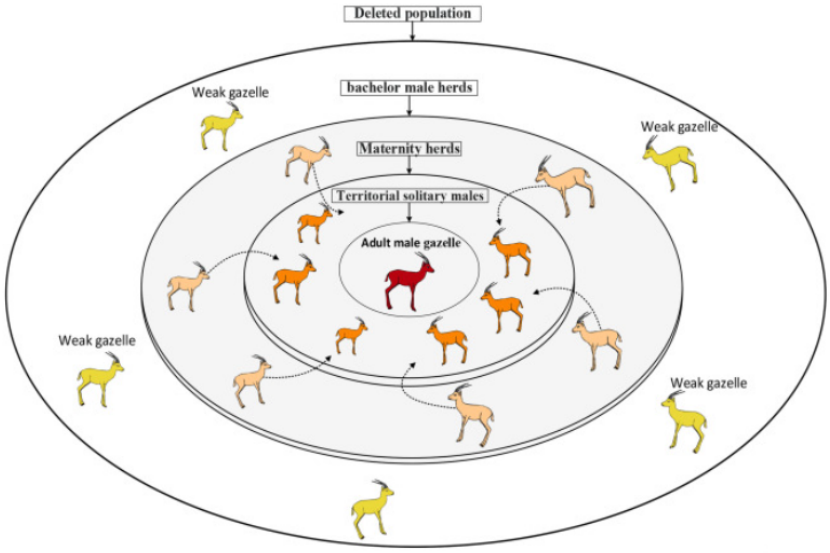


Figure II.2: Optimization Procedure of the Mountain Gazelle Optimizer [28].

II.3.2 Mountain Gazelle Optimizer Flowchart

The TSM, MH, BMH, and MSF mechanisms are applied to all gazelles to generate new Generations. After each complete cycle, the gazelles are ranked, and the best ones, with high-quality and low-cost solutions, are kept while the old and weak ones are removed from the population. The best gazelle is the adult male who owns the territory. The MGO general flowchart is depicted in Figure II.3. MGO can make optimization

more accessible to engineers and designers who may not have specialized knowledge in optimization techniques by being easier to use or implement than existing methods [27].

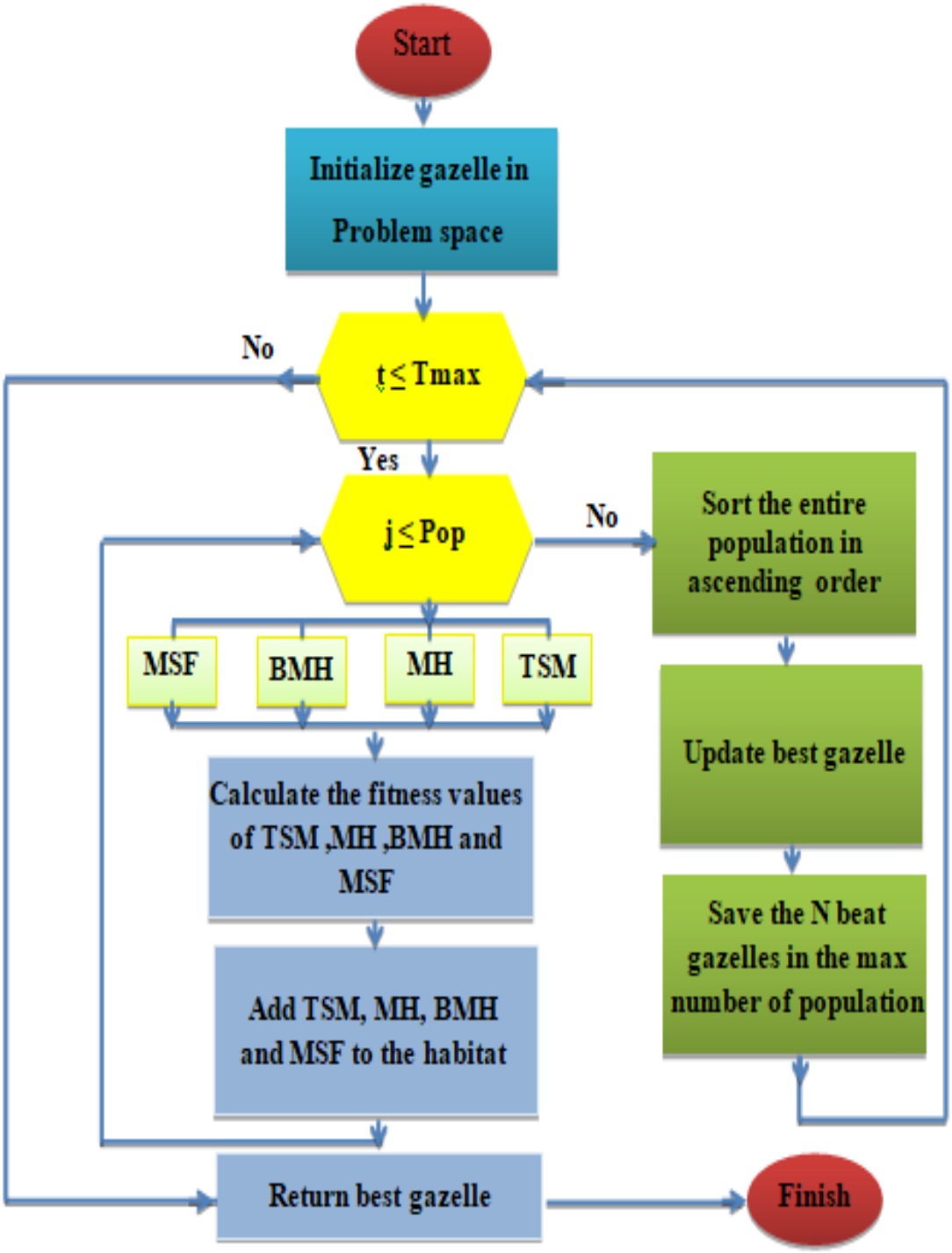


Figure II.3: Mountain Gazelle Optimizer Flowchart [27].

II.3.3 Pseudo code of Mountain Gazelle Optimizer

Algorithm II.1: Mountain Gazelle Optimization (MGO) [27].

Input Population size N and the maximum number of iterations
Output Gazelle's location and fitness potential
Create a random population using $X_i (i = 1, \ldots, N)$;
Calculate gazelle's fitness levels;
while *the stopping condition is not met* **do**
  for *each gazelle* X_i **do**
    Calculate TSM using **Eq II.1**;
    Calculate MH using **Eq II.6**;
    Calculate BMH using **Eq II.7**;
    Calculate MSF using **Eq II.9**;
    Calculate the fitness values of TSM, MH, BMH, and MSF and add to the habitat;
  end
  Sort the entire population in ascending order;
  Update $best_{\text{gazelle}}$;
  Save the $best_{\text{gazelle}}$ in the maximum number of population;
end
return $X_{\text{best gazelle}}$;

II.4 Red-Tailed Hawk Algorithm (RTH)

This study suggests a new nature-inspired metaheuristic optimization algorithm called the Red-tailed Hawk algorithm (RTH). As a predator, the Red-tailed Hawk has a hunting strategy from detecting the prey until the swoop stage. There are three stages during the hunting process. In the high soaring stage, the Red-tailed Hawk explores the search space and determines the area with the prey location. In the low soaring stage, the Red-tailed Hawk moves inside the selected area around the prey to choose the best position for the hunt. Then, the Red-tailed Hawk swings and hits its target in the stooping and swooping stages. The proposed algorithm mimics the prey hunting method of the Red-tailed Hawk for solving real world optimization problems [29].

II.4.1 Inspiration and Behavior During Hunting

The Red-tailed Hawk (*Buteo jamaicensis*) is a bird of prey found across North America, from Alaska and Canada to Panama and the West Indies. It adapts to various

habitats, including deserts, grasslands, forests, farms, and cities. A carnivore, it mainly feeds on small mammals like rodents, which make up 85% of its diet, but also eats birds, reptiles, amphibians, fish, and invertebrates, depending on location and season.

It soars with slightly raised wings, flapping minimally to conserve energy, enabling long-distance flight. While gliding or flapping, it travels at (32–64 km/h) (20–40 mph), and can dive at speeds up to (190 km/h) (120 mph). During nest defense, it dives rapidly at threats with great speed and force. As illustrated in Figure II.4, the Red-tailed Hawk demonstrates specialized behavior during hunting [29].



Figure II.4: Behavior of Red-tailed Hawk during hunting [29].

High Soaring (Figure II.4 a): The Red-tailed Hawk flies at a high altitude with its wings in a mild dihedral, flapping as little as possible to conserve energy while exploring the selected area.

Low Soaring (Figure II.4 b): After selecting the target position, the Red-tailed Hawk soars at a lower altitude in a spiral movement around the prey. This maneuver allows it to identify the best location and timing to strike.

Stooping and Swooping (Figure II.4 c): Once the optimal position and moment are determined, the Red-tailed Hawk swoops toward its prey by stooping—rapidly accelerating from (64 km/h to 190 km/h) in a curved trajectory [29].

II.4.2 Mathematical Model

The suggested Red-tailed Hawk (RTH) algorithm mimics the Red-tailed Hawk's hunting behavior. The actions taken at each hunt stage are presented and modeled. This algorithm includes three stages, high soaring, low soaring, stooping and swooping [29].

II.4.2.1 High Soaring

The Red-tailed Hawk will soar far into the sky, looking for the best location in terms of food availability. Figure II.5 illustrates the behavior of the Red-tailed Hawks during the high soaring stage and Eq II.10 represents the mathematical model of this stage.

$$X(t) = X_{\text{best}} + \big(X_{\text{mean}} - X(t-1)\big) \cdot \text{Levy}(\text{dim}) \cdot \text{TF}(t) \tag{II.10}$$

Where X (t) represents the Red-tailed Hawk's position at iteration t, X_{best} is the best obtained position, X_{mean} is the position's mean, Levy represents the Levy flight distribution function that can be calculated according to Eq II.11, and $TF(t)$ denotes the transition factor function that can be calculated according to Eq II.12

$$\begin{cases} Levy(\text{dim}) = s \cdot \frac{u \cdot \sigma}{|v|^{\beta-1}} \\ \sigma = \left(\frac{T(1+\beta) \cdot \sin\left(\frac{\pi\beta}{2}\right)}{T\left(1+\frac{\beta}{2}\right) \cdot \beta \cdot 2^{(1-\frac{\beta}{2})}} \right) \end{cases} \tag{II.11}$$

where s is a constant ($s = 0.01$), dim is the problem dimension, β is a constant ($\beta = 1.5$), and u , v are random numbers uniformly distributed in the interval $[0, 1]$.

$$\text{TF(t)} = 1 + \sin\left(2.5 + \frac{t}{T_{\max}}\right) \tag{II.12}$$

Where $T_{\max}$ represents the maximum number of iterations [29].

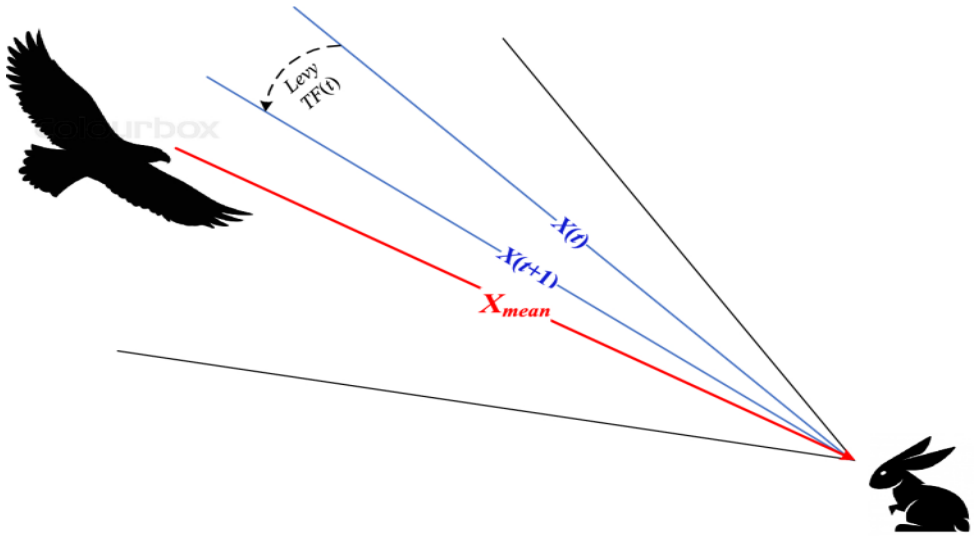


Figure II.5: Behavior of Red-tailed Hawk during high soaring stage [29].

II.4.2.2 Low Soaring

The hawk surrounds the prey by flying much lower to the ground in a spiral line. This stage is illustrated in Figure II.6, and its model can be expressed as follows:

$$\begin{cases} X(t) = X_{\text{best}} + (x(t) + y(t)) \cdot \text{stepsize}(t) \\ \text{stepsize}(t) = X(t) - X_{\text{mean}} \end{cases} \tag{II.13}$$

where x and y denote directional coordinates, which can be calculated as follows:

$$\begin{cases} x(t) = R(t) \cdot \sin(\theta(t)) \\ y(t) = R(t) \cdot \cos(\theta(t)) \end{cases} \quad \begin{cases} R(t) = R_0 \cdot \left(r - \dfrac{t}{T_{\max}}\right) \cdot \text{rand} \\ \theta(t) = A \cdot \left(1 - \dfrac{t}{T_{\max}}\right) \cdot \text{rand} \end{cases} \quad \begin{cases} x(t) = \dfrac{x(t)}{\max|x(t)|} \\ y(t) = \dfrac{y(t)}{\max|y(t)|} \end{cases} \tag{II.14}$$

where R_0 represents the initial value of the radius $[0.5,\ 3]$, A denotes the angle gain $[5,\ 15]$, rand is a random gain $[0,\ 1]$, and r is a control gain $[1,\ 2]$. These parameters help the hawk fly around the prey in spiral movements [29].

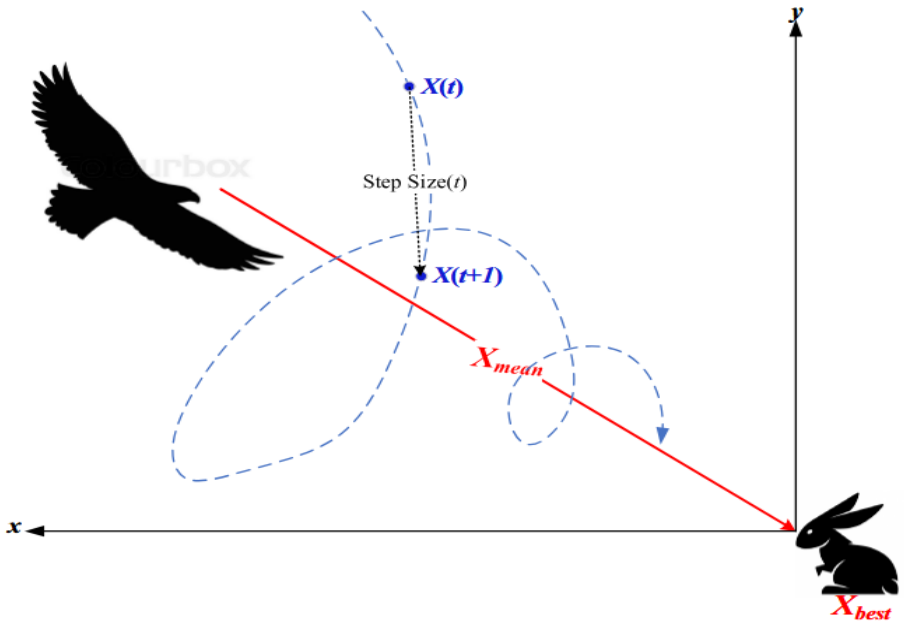


Figure II.6: Behavior of red-tailed hawk during low soaring stage [29].

II.4.2.3 Stooping and Swooping

In this stage, the hawk suddenly stoops and attacks the prey from the best-obtained position in the low soaring stage. Figure II.7 explains the behavior of the Red-tailed

Hawks during this stage. This stage can be modelled as follows:

$$X(t) = \alpha(t) \cdot X_{\text{best}} + x(t) \cdot \text{stepsize1}(t) + y(t) \cdot \text{stepsize2}(t) \tag{II.15}$$

Where each stepsize can be calculated as follows:

$$\begin{cases} \text{stepsize1}(t) = X(t) - TF(t) \cdot X_{\text{mean}} \\ \text{stepsize2}(t) = G(t) \cdot X(t) - TF(t) \cdot X_{\text{best}} \end{cases} \tag{II.16}$$

where α and G are the acceleration and gravity factors, respectively. They can be defined as follows:

$$\begin{cases} \alpha(t) = \sin^2\left(2.5 - \dfrac{t}{T_{\max}}\right) \\ G(t) = 2\left(1 - \dfrac{t}{T_{\max}}\right) \end{cases} \tag{II.17}$$

where α represents the hawk's acceleration, which increases with time t to enhance convergence speed, and G is the gravity effect, which decreases as the hawk approaches the prey to reduce exploitation diversity [29].

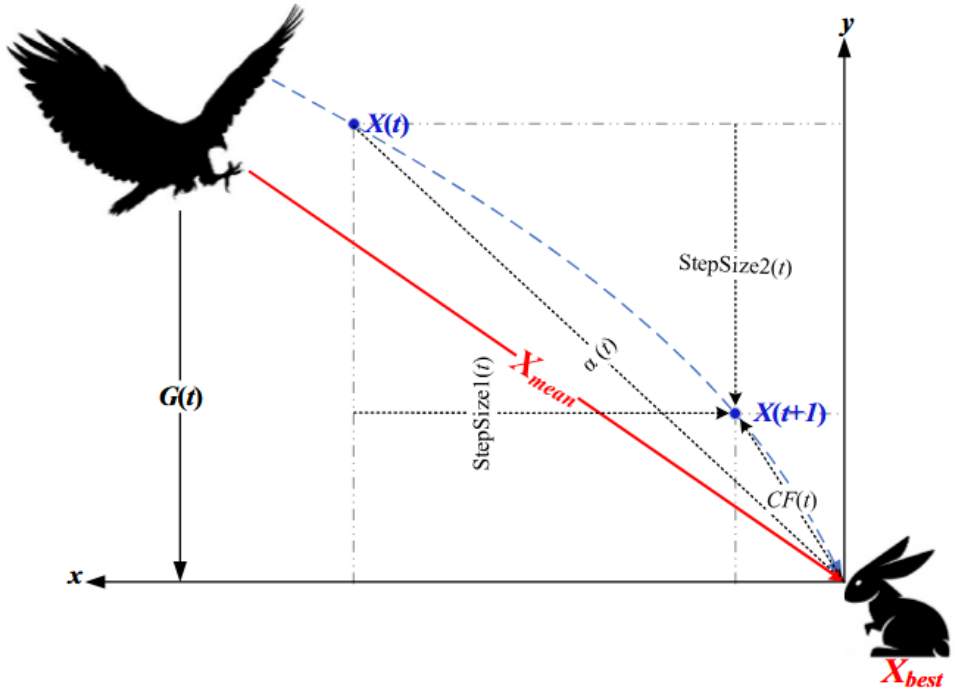


Figure II.7: Behavior of red-tailed hawk during stooping and swooping stages [29].

II.4.3 Pseudo code of Red-Tailed Hawk

Algorithm II.2: Red-tailed Hawk Optimization (RTH) [29].

Input: Search space, maximum iterations $T_{\max}$, population size N_{pop}
Output: Best solution found
Initialization: random generation within the search space;
while $t < T_{\max}$ **do**
  High soaring stage: for $i = 1$ **to** N_{pop} **do**
    Calculate Lévy flight distribution **Eq II.11**;
    Calculate the transition factor TF **Eq II.12**;
    Update position **Eq II.10**;
  end
  Low soaring stage: for $i = 1$ **to** N_{pop} **do**
    Calculate direction coordinates **Eq II.14**;
    Update position **Eq II.13**;
  end
  Stooping and swooping stage: for $i = 1$ **to** N_{pop} **do**
    Calculate the acceleration and the gravity factors **Eq II.17**;
    Calculate the step size **Eq II.16**;
    Update positions **Eq II.15**;
  end
end

II.5 Dung Beetle Optimizer (DBO)

The Dung Beetle Optimizer (DBO) is a nature-inspired metaheuristic algorithm based on the behavior of dung beetles, including ball rolling, dancing, foraging, stealing, and reproduction. It balances global exploration and local exploitation, offering high convergence speed and accuracy. The algorithm has shown strong performance on benchmark functions and real-world engineering problems, outperforming many existing optimization techniques [30].

II.5.1 Inspiration

It is well known that the dung beetle, as a common insect in nature, feeds on the dung of animals. Note that dung beetles are found in most parts of the world and act as decomposers in nature; this means that they are of vital importance in the ecosystem. Research has shown that dung beetles have an interesting habit of making dung into a

ball and then rolling it away, as captured in Figure II.8. It is worth mentioning that the purpose of dung beetles is able to move their dung ball as quickly and efficiently as possible, which can prevent them from being competed by other dung beetles.

In the next subsection, the behavior of the dung beetle will be modeled mathematically, with the aim of developing an optimizer that exhibits satisfactory search performance [30].

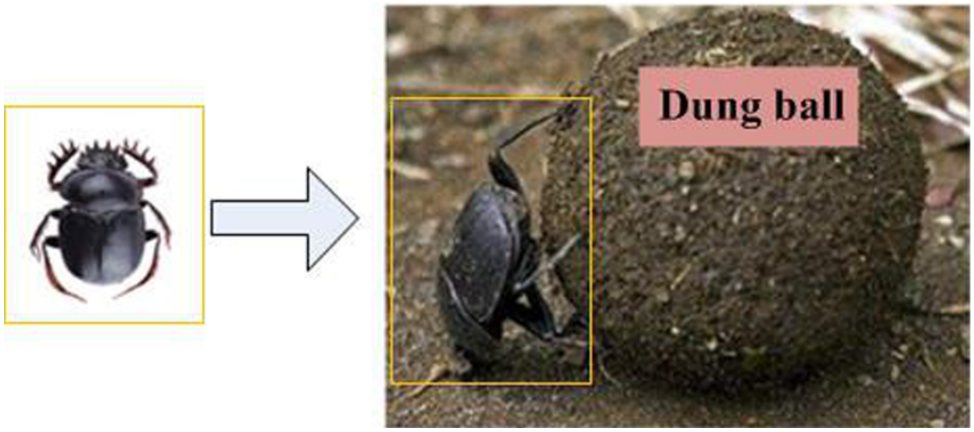


Figure II.8: The rolling dung ball behavior of the dung beetle [30].

II.5.2 Mathematical Model

II.5.2.1 Roll-Ball Dung Beetle

The roll-ball dung beetle navigates with the sun to ensure the dung ball rolls in a Straight path. Natural factors like light intensity and wind can influence the roll-ball dung Beetle's trajectory. The position update for the roll-ball dung beetle can be expressed as follows:

$$\begin{cases} X_i(t) = X_i(t) \times \alpha \times K \times X_i(t-1) + b \times \Delta_x \\ \Delta_x = |X_i(t) - X^{\omega}| \end{cases} \tag{II.18}$$

Where t represents the current iteration number; $X_i(t)$ represents the position information of the i^{th} dung beetle at the t^{th} iteration; α is a natural coefficient that indicates whether to deviate from the original direction, and is assigned either -1 or 1 based on probability; $K \in (0, 0.2)$ represents the deviation coefficient; $b \in (0, 1)$ is a constant, with K and b set to 0.1 and 0.3, respectively; X^{ω} denotes the global worst position; and Δ_x is used to simulate changes in light intensity.

The updated formula for the dancing position of a dung beetle on a dung ball, when it encounters an obstacle and needs to choose a new route to continue moving forward, is represented as follows:

$$X_i(t+1) = X_i(t) + \tan(\theta) \cdot |X_i(t) - X_i(t-1)| \tag{II.19}$$

Where $\theta \in [0, \pi]$ represents the deviation angle, and when $\theta = 0$, $\frac{\pi}{2}$, or π, the position of the dung beetle will not be updated [31].

II.5.2.2 Brood Ball

The brood ball utilizes a boundary selection strategy to simulate the oviposition area of a female dung beetle. The definition of the oviposition area is as follows:

$$\begin{cases} Lb^* = \max\left(X^*(1-R), Lb\right) \\ Ub^* = \min\left(X^*(1+R), Ub\right) \end{cases} \tag{II.20}$$

Where X^* represents the current local best position; Lb^* , Ub^* represent the lower and upper bounds of the oviposition area, respectively; $R = 1 - \frac{t}{T_{\max}}$, where $T_{\max}$ represents the maximum number of iterations; and Lb , Ub represent the lower and upper bounds of the optimization problem.

As indicated by the above formula, the oviposition area is dynamically changing. Therefore, during the iteration process, the position of the brood ball is also dynamically changing. The position of the brood ball is defined as follows:

$$B_i(t+1) = X^* + b_1 \times \left(B_i(t) - Lb^*\right) + b_2 \times \left(B_i(t) - Ub^*\right) \tag{II.21}$$

Where $B_i(t)$ represents the position information of the i^{th} brood ball during the t^{th} iteration; b_1 , b_2 are two independent random vectors of size $1 \times D$; and D represents the dimension of the optimization problem [31].

II.5.2.3 Scout Dung Beetle

After being born, the scout dung beetle searches for food in the best foraging area. The definition of the best foraging area is as follows:

$$\begin{cases} Lb^b = \max\left(X^b \times (1-R), Lb\right) \\ Ub^b = \max\left(X^b \times (1+R), Ub\right) \end{cases} \tag{II.22}$$

Where X^b represents the current local best position, and Lb^b , Ub^b represent the lower and upper bounds of the best foraging area. Therefore, the position of the scout dung beetle is updated as follows:

$$X_i(t+1) = X_i(t) + C_1 \times \left(X_i(t) - Lb^b\right) + C_2 \times \left(X_i(t) - Ub^b\right) \tag{II.23}$$

Where $X_i(t)$ represents the position information of the i^{th} scout dung beetle during the t^{th} iteration, C_1 represents a random number following a normal distribution, and $C_2 \in (0, 1)$ represents a random vector [31].

II.5.2.4 Thief Dung Beetle

The thief dung beetle steals dung balls from other dung beetles. As derived from the above equation, X^b is the best location for competing for food. Therefore, the position information of the thief dung beetle is updated as follows:

$$X_i(t) = X^b + s \times g \times \left(|X_i(t) - X^*| + |X_i(t) - X^b|\right) \tag{II.24}$$

Where $X_i(t)$ represents the position information of the i^{th} thief dung beetle during the t^{th} iteration, g represents a random vector of size $1 \times D$ following a normal distribution, and s represents a constant value [31].

II.5.3 Dung Beetle Optimization Flowchart

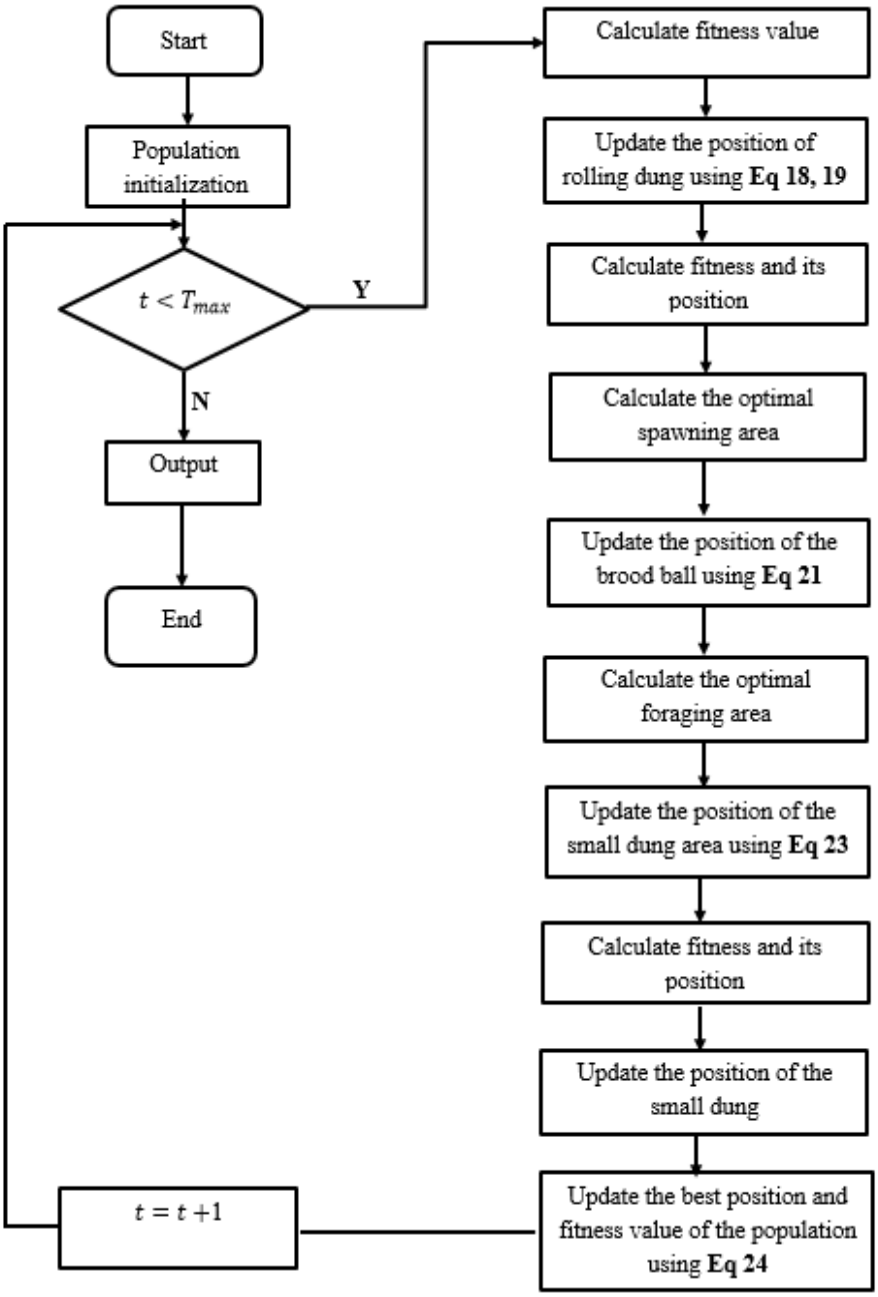


Figure II.9: Flowchart of the dung beetle optimization algorithm [31].

II.5.4 Pseudo code Dung Beetle Optimization

Algorithm II.3: Dung Beetle Optimization (DBO) [32].

Set the population size N and the maximum iterations T_{max} ;
Initialize the particles D_i $(i = 1, 2, \ldots, N)$ and classify the populations;
while $t < T_{max}$ **do**
  for $i \leftarrow 1$ **to** N **do**
    if $i ==$ *Rolling Dung Beetle* **then**
      $\delta = rand(1)$;
      if $\delta < 0.9$ **then**
        Updating the Rolling Dung Beetle with **Eq II.18**;
      end
      else
        Updating the Rolling Dung Beetle with **Eq II.19**;
      end
    end
    if $i ==$ *brood Ball* **then**
      Updating the location of breeding dung beetles using **Eq II.21**;
    end
    if $i ==$ *Scout Dung Beetles* **then**
      Updating the location of the small dung beetle using **Eq II.23**;
    end
    if $i ==$ *Theif Dung Beetles* **then**
      Updating the location of the stealing dung beetle using **Eq II.24**;
    end
  end
  Making greedy choices;
  $t \leftarrow t + 1$;
end

II.6 Arctic Puffin Optimization (APO)

The Arctic Puffin Optimization (APO) algorithm was proposed by Wang et al. [33] in September 2024. Originating from the survival strategies of Arctic puffins in nature, the APO algorithm is inspired by their flight and foraging behaviors. The APO algorithm boasts strong optimization capabilities, few parameters, and a simple principle, making it highly competitive in performance compared to other intelligent optimization algorithms.

II.6.1 Inspiration

The Arctic puffin is a rare and small bird endemic to the Arctic. They typically inhabit the oceans and usually forage in groups or flocks, exhibiting excellent fishing skills and flight abilities while working collaboratively to forage in the ocean. Arctic puffins prefer to fly in clusters near the edge of the ocean, swimming at the surface and feeding on fish. Compared to other seabirds, the Arctic puffin has short, stubby wings and maintains flight at low altitudes by rapidly flapping its tiny wings [33].

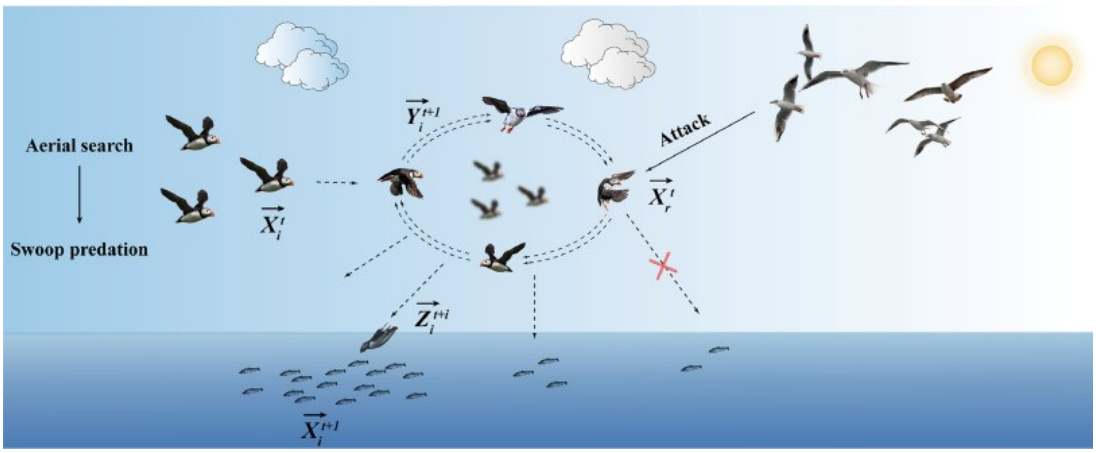


Figure II.10: Aerial flight stage of the Arctic puffin [33].

II.6.2 Mathematical Model

The mathematical model of the APO algorithm is primarily composed of three stages: the population initialization phase, the aerial flight phase, and the underwater foraging phase [34].

II.6.2.1 Initial Population

The specific behaviors of Arctic puffins in the air and on the water form the basis for the design of the APO algorithm. The APO algorithm initializes the population using the following formula:

$$\vec{X}_i^t = \text{rand} \times (ub - lb) + lb, \quad i = 1, 2, 3, \ldots, N \tag{II.25}$$

Where $\vec{X}_i^t$ represents the position of the i^{th} Arctic puffin; `rand` is a random number between 0 and 1; ub , lb represent the upper and lower bounds, respectively; and N is the population size [34].

II.6.2.2 Aerial Flight Stage

The Arctic puffins rely on unique flying and foraging strategies to cope with their challenging survival. In their daily lives, they must adapt flexibly between the ocean and the air, meet their nutritional needs, and adjust to different environments. During the aerial foraging phase, the Arctic Puffin employs two key strategies to address different situations, namely the aerial search strategy and the swooping predation strategy.

The first strategy is aerial search

The aerial search strategy simulates the behavior of the Arctic Puffin searching for suitable foraging waters while in the air, utilizing Levy flight as its powerful wings to change position. When encountering predators such as seagulls, it employs a spiral flight strategy to evade the predators. The following is the position update formula [34]:

$$\vec{Y}_r^{(t+1)} = \vec{X}_i^t + \left(\vec{X}_i^t - \vec{X}_r^t\right) \times L(D) + R \tag{II.26}$$

$$R = \text{round}\left(0.5 \times (0.5 + \text{rand})\right) \times \alpha \tag{II.27}$$

$$\alpha \sim \ Normal(0, 1) \tag{II.28}$$

Where R is a random integer between 1 and $N-1$, excluding i; $\vec{X}_i^t$ represents the current i^{th} candidate solution in the population; $\vec{X}_r^t$ is a candidate solution randomly selected from the current population, with $\vec{X}_i^t \neq \vec{X}_r^t$; $L(D)$ denotes a random number generated through the Lévy flight mechanism; D is the dimensionality of the problem; and α is a random number following a standard normal distribution [34].

The second strategy is swooping predation

The swooping predation strategy simulates the behavior of the Arctic Puffin, rapidly changing its flight direction to dive and feed upon spotting prey. To ensure their survival, they must ensure faster and more successful capture of their prey. To simulate this diving behavior, the algorithm introduces a velocity coefficient S to adjust the displacement of the Arctic Puffin during the dive process. The following is the position update formula:

$$\vec{Z}_i^{(t+1)} = \vec{Y}_i^{(t+1)} \times S \tag{II.29}$$

$$S = \tan\left((\text{rand} - 0.5) \times \pi\right) \tag{II.30}$$

To achieve the best results under various conditions, the algorithm combines the candidate positions generated by the two strategies, sorts them based on their fitness values, and selects the top N individuals with the best fitness values to form a new population. The equation describing this process is as follows [34]

$$\vec{P}_i^{(t+1)} = \vec{Y}_i^{(t+1)} \cup \vec{Z}_i^{(t+1)} \tag{II.31}$$

$$\text{new} = \text{sort}\left(\vec{P}_i^{(t+1)}\right) \tag{II.32}$$

$$\vec{X}_i^{(t+1)} = \text{new}(1:N) \tag{II.33}$$

II.6.2.3 Underwater Foraging Stage

The survival strategy of the Arctic puffin involves two crucial aspects: aerial flight and underwater foraging. The underwater foraging phase consists of three main strategies, each employed under specific circumstances to enhance predation efficiency. These strategies are gathering, foraging, intensifying search, and avoiding predators [34].

The first strategy is gathering foraging

The gathering foraging strategy simulates the cooperative foraging behavior of Arctic puffins, and the following equation describes the location update:

$$\vec{W}_i^{(t+1)} = \begin{cases} \vec{X}_{r_1}^t + F \cdot L(D) \cdot \left(\vec{X}_{r_2}^t - \vec{X}_{r_3}^t\right), & \text{if rand} \geq 0.5 \\ \vec{X}_{r_1}^t + F \cdot \left(\vec{X}_{r_2}^t - \vec{X}_{r_3}^t\right), & \text{if rand} < 0.5 \end{cases} \tag{II.34}$$

Where F represents the cooperative factor, adjusting the predation behavior of Arctic puffins. In this paper, $F = 0.5$. The variables r_1, r_2, r_3 are random integers between 1 and $N-1$ (excluding i), and $\vec{X}_{r_1}^t, \vec{X}_{r_2}^t, \vec{X}_{r_3}^t$ are candidate solutions randomly selected from the current population, with $r_1 \neq r_2 \neq r_3$ and $\vec{X}_{r_2}^t \neq \vec{X}_{r_3}^t$.

In Eq II.34, when rand < 0.5, it represents the cooperative foraging behavior of the Arctic puffin with other members, utilizing a cooperation factor F and engaging in random motion to explore the surrounding environment. When rand ≥ 0.5, it signifies a more complex food search strategy where the Arctic puffin initially follows other members and, upon discovering a school of fish, quickly swims to join a more advantageous predatory group [34].

The second strategy is intensifying the search

The intensified search strategy describes a situation where, as predation proceeds, the food resources in the current foraging area gradually become depleted. To continue meeting their needs, Arctic puffins must change their underwater position to seek out new food sources. The position update equation for this phase is as follows:

$$\vec{Y}_i^{(t+1)} = \vec{W}_i^{(t+1)} \times (1 + f) \tag{II.35}$$

$$f = 0.1 \times (\text{rand} - 1) \times \frac{T_{max} - t}{T_{max}} \tag{II.36}$$

Where f is an adaptive factor used to adjust the position of the Arctic puffin in the water. T_{max} represents the total number of iterations, and t denotes the current iteration count.

The third strategy is avoiding predators

The avoiding predator strategy is used to describe the behavior of an Arctic puffin when it spots a nearby predator, and here is the location update equation used for this strategy [34]:

$$\vec{Z}_i^{(t+1)} = \begin{cases} \vec{X}_{r_1}^t + F \cdot L(D) \cdot \left(\vec{X}_{r_1}^t - \vec{X}_{r_2}^t\right), & \text{if rand} \geq 0.5 \\ \vec{X}_{r_1}^t + \beta \cdot \left(\vec{X}_{r_1}^t - \vec{X}_{r_2}^t\right), & \text{if rand} < 0.5 \end{cases} \tag{II.37}$$

Where β is a uniformly distributed number between 0 and 1.

To achieve the best results under various conditions, the algorithm merges the candidate positions generated by the three strategies, sorts them based on their fitness values, and selects the top N individuals with the superior fitness values to form a new population. The equation describing this process is as follows [34]:

$$\vec{P}_i^{(t+1)} = \vec{W}_i^{(t+1)} \cup \vec{Y}_i^{(t+1)} \cup \vec{Z}_i^{(t+1)} \tag{II.38}$$

$$\text{new} = \text{sort}\left(\vec{P}_i^{(t+1)}\right) \tag{II.39}$$

$$\vec{X}_i^{(t+1)} = \text{new}(1 : N) \tag{II.40}$$

II.6.2.4 Behavior Conversion Factor B

The APO algorithm favors aerial foraging for global search in the early stages of iteration and underwater foraging for local exploitation in the later stages. This search mechanism is derived from the natural behavior of the Arctic puffin, which initially searches for suitable foraging waters in the air and then primarily forages underwater. To achieve a smooth transition from global search to local exploitation, the algorithm incorporates a behavior conversion factor, denoted as B. Here is its definition:

$$B = 2 \times \log\left(\frac{1}{\text{rand}}\right) \times \left(1 - \frac{t}{T_{max}}\right) \tag{II.41}$$

The value of B can be dynamically adjusted as the iterations progress to accommodate the exploration needs at different stages. Additionally, a parameter C is introduced within the algorithm to determine the strategy to be executed at the current iteration stage by comparing the values of B and C. In this study, the parameter C is set to 0.5 [34].

II.6.3 Pseudo code of Arctic Puffin Optimizer

Algorithm II.4: Arctic Puffin Optimization (APO) [34].

Input: N, T, D, F, and C
Output: The best $\vec{X}_i^t$ and its fitness value
Initialize N puffins, $\vec{X}_i^t$ $(i = 1, 2, \ldots, N)$ using **Eq II.25**;
Evaluate each $\vec{X}_i^t$ and find the one with the best fitness;
$t \leftarrow 1$;
while $t < T_{max}$ **do**
  Calculate the behavior conversion factor B according to **Eq II.41**;
  if $B > C$ **then**
    `// Air flight period (Exploration phase)`
    for $i = 1$ **to** N **do**
      Update $\vec{Y}_i^{t+1}$ using **Eq II.26** ; `// Air search`
      Update $\vec{Z}_i^{t+1}$ using **Eq II.29** ; `// Dive predation`
      Select N excellent populations as the new population $\vec{X}_i^{t+1}$ using **Eq II.31** to **Eq II.33**;
      Evaluate the puffins $\vec{X}_i^{t+1}$ and replace $\vec{X}_i^t$ with $\vec{X}_i^{t+1}$ if it is better;
    end
  else
    `// Diving and foraging period (Exploitation phase)`
    for $i = 1$ **to** N **do**
      Update $\vec{W}_i^{t+1}$ using **Eq II.34** ; `// Gather for food`
      Update $\vec{Y}_i^{t+1}$ using **Eq II.35** ; `// Strengthen search`
      Update $\vec{Z}_i^{t+1}$ using **Eq II.37** ; `// Avoid predators`
      Select N excellent populations as the new population $\vec{X}_i^{t+1}$ using **Eq II.38** to **Eq II.40**;
      Evaluate the puffins $\vec{X}_i^{t+1}$ and replace $\vec{X}_i^t$ with $\vec{X}_i^{t+1}$ if it is better;
      $t \leftarrow t + 1$;
    end
  end
end
return $\vec{X}_i^t$

II.7 Conclusion

In this chapter, a comprehensive overview of metaheuristic optimization algorithms was presented [35], highlighting their increasing significance in addressing complex, real-world problems where traditional methods often prove inadequate. The chapter categorized metaheuristics based on their sources of inspiration, determinism, search strategies, and population dynamics. Several state-of-the-art algorithms were introduced and examined in detail, including Mountain Gazelle Optimizer (MGO),the Red-tailed Hawk Algorithm (RTH), Dung Beetle Optimizer (DBO), and Arctic Puffin Optimization (APO).

Each algorithm was discussed in terms of its biological or behavioral inspiration, core characteristics, and mathematical modeling. These algorithms illustrate the potential of nature-inspired intelligence to effectively tackle a wide range of optimization challenges.

Chapter III

Results and Discussion

III.1 Introduction

This chapter presents and explains in detail the simulation results of four meta-heuristic algorithms: Mountain Gazelle Optimizer (MGO), Red-tailed Hawk Optimizer (RTH), Dang Beetle Optimizer (DBO), and Arctic Puffin Optimization (APO), to determine the electrical parameters of single- and dual-diode solar photovoltaic models of an RTC France silicon solar cell. These parameters are estimated using Newton-Raphson and W-Lambert techniques via MATLAB simulations. The results highlight the proposed approach's flexibility and convergence efficiency of the aforementioned models.

III.2 Methods for Estimating PV Module Parameters

Various techniques have been proposed in recent years to extract parameters from photovoltaic. These techniques can be classified into three broad categories: analytical (Lambert-W function) [36], iterative (Newton-Raphson method) [37], and intelligent methods (Particle Swarm Optimization (PSO), Genetic Algorithms (GA)) [38]. Literature reviews indicate that the accuracy of the results varies depending on the method employed.

III.2.1 Analytical Methods

Analytical methods are widely used for estimating PV module parameters. These methods explicitly solve analytical equations, reducing computational time since a single equation is often sufficient to determine a parameter [39]. Their effectiveness has been demonstrated for certain solar module models, with some approaches recommending the use of the Lambert-W function.

Femia et al. [40] proposed an analytical method for calculating the series resistance Rs and parallel resistance Rp using the Lambert-W function. This approach explicitly defines the PV module's output current in terms of voltage, showcasing strong performance. Likewise, Batzelis et al. [41] expressed voltage as a function of current based on the Lambert-W function.

The Lambert-W function

The Lambert-W function is a powerful mathematical tool that enables the analytical resolution of certain equations. Its application in modeling non-ideal junctions with series resistance Rs and shunt resistance Rsh in solar cell characteristics highlights its advantages. The analytical solution provided by the Lambert-W function offers a general description of the physical problem's behavior, unlike numerical solutions, which depend on specific values.

Moreover, the Lambert-W function helps unify various phenomena by providing an exact solution, avoiding the convergence issues often encountered with numerical methods. Its ability to be integrated and differentiated enhances the understanding of physical behaviors as equation parameters change.

The history of the Lambert-W function dates back to 1758 when it was introduced by Lambert, later studied by Euler in 1779, and formally named in 1959 following the work of E.M. Wright. Its widespread use across different applications demonstrates its significance and robustness in solving complex physical problems.

The Lambert-W function is defined as the function that satisfies the following formula:

$$Z = W(X)\, e^{W(X)} \tag{III.1}$$

With:

Z: Represents the argument of the function W.

$e^{(X)}$: Represents the exponential function, and X is a complex or real vector.

Therefore, the vector X is obtained in the form $X = (Z)$.

Applying the Lambert-W function to the equation will allow us to simplify the calculation of the predicted current I_{pv}.

$$(R_{\text{sh}} + R_s)I_L = R_{\text{sh}}I_K - R_{\text{sh}}I_{\text{sd}}\, e^{\left(\frac{V_L + R_s I_L}{n \cdot V_t}\right)} - V_L \tag{III.2}$$

Where I_K is defined by $I_K = I_{\text{ph}} + I_{\text{sd}}$

Then, by multiplying both sides of Eq III.2 by the term ($\frac{R_s}{R_{\text{sh}}+R_s}$), we obtain:

$$R_s I_L = \frac{R_s}{R_{\text{sh}} + R_s}\left(R_{\text{sh}}I_K - R_{\text{sh}}I_{\text{sd}}\, e^{\left(\frac{V_L + R_s I_L}{n \cdot V_t}\right)} - V_L\right) \tag{III.3}$$

Then, the term Vpv is added in both members of Eq III.3. Then, by dividing the equation obtained by the term $(n \cdot V_t)$, we obtain:

$$\frac{V_L + R_s I_L}{n \cdot V_t} = \frac{R_s}{n \cdot V_t(R_{\text{sh}} + R_s)}\left(R_{\text{sh}}I_K - R_{\text{sh}}I_{sd}\, e^{\left(\frac{V_L + R_s I_L}{n \cdot V_t}\right)} + \frac{R_{\text{sh}}}{R_s}V_L\right) \tag{III.4}$$

Now, Eq III.4 is simplified again, thus giving the following equation:

$$\left(\begin{array}{l} \dfrac{V_L + R_s I_L}{n \cdot V_t} + \dfrac{R_s R_{\text{sh}} I_{\text{sd}}}{n \cdot V_t(R_{\text{sh}} + R_s)}\, e^{\left(\frac{V_L + R_s I_L}{n \cdot V_t}\right)} \\ \quad = \dfrac{R_s}{n \cdot V_t(R_{\text{sh}} + R_s)}\left(R_{\text{sh}}I_K + \dfrac{R_{\text{sh}}}{R_s}V_L\right) \end{array}\right) \tag{III.5}$$

Then, the exponential function of both sides of Eq III.5 is calculated, and the result is multiplied by the term ($\frac{R_s R_{\text{sh}} I_{\text{sd}}}{n \cdot V_t (R_{\text{sh}}+R_s)}$). Hence, the resulting equation is given by:

$$\left(\begin{array}{c} \dfrac{R_s R_{\text{sh}} I_{\text{sd}}}{n \cdot V_t (R_{\text{sh}}+R_s)} e^{\left(\frac{V_L + R_s I_L}{n \cdot V_t}\right)} e^{\left(\frac{R_s R_{\text{sh}} I_{\text{sd}}}{n \cdot V_t (R_{\text{sh}}+R_s)} e^{\left(\frac{V_L + R_s I_L}{n \cdot V_t}\right)}\right)} \\ = \dfrac{R_s R_{\text{sh}} I_{\text{sd}}}{n \cdot V_t (R_{\text{sh}}+R_s)} e^{\left(\frac{R_s}{n \cdot V_t (R_{\text{sh}}+R_s)} \left(R_{\text{sh}} I_K + \frac{R_{\text{sh}}}{R_s} V_L\right)\right)} \end{array} \right) \tag{III.6}$$

Taking the Lambert-W function of both sides of Eq III.6, we obtain:

$$\left(\begin{array}{c} \dfrac{R_s R_{\text{sh}} I_{\text{sd}}}{n \cdot V_t (R_{\text{sh}}+R_s)} e^{\left(\frac{V_L + R_s I_L}{n \cdot V_t}\right)} = \\ \text{LambertW}\left(\dfrac{R_s R_{\text{sh}} I_{\text{sd}}}{n \cdot V_t (R_{\text{sh}}+R_s)} e^{\left(\frac{R_s}{n \cdot V_t (R_{\text{sh}}+R_s)} \left(R_{\text{sh}} I_K + \frac{R_{\text{sh}}}{R_s} V_L\right)\right)} \right) \end{array} \right) \tag{III.7}$$

Now, Eq III.7 is simplified again, thus giving the following equation:

$$\left(\begin{array}{c} R_{\text{sh}} I_{\text{sd}} \, e^{\left(\frac{V_L + R_s I_L}{n \cdot V_t}\right)} = \dfrac{n \cdot V_t (R_{\text{sh}}+R_s)}{R_s} \\ \text{LambertW}\left(\frac{R_s R_{\text{sh}} I_{\text{sd}}}{n \cdot V_t (R_{\text{sh}}+R_s)} \, e^{\left(\frac{R_s}{n \cdot V_t (R_{\text{sh}}+R_s)} \left(R_{\text{sh}} I_K + \frac{R_{\text{sh}}}{R_s} V_L\right)\right)} \right) \end{array} \right) \tag{III.8}$$

According to Eq III.8, the term is rewritten as:

$$R_{\text{sh}} I_{\text{sd}} \, e^{\left(\frac{V_L + R_s I_L}{n \cdot V_t}\right)} = R_{\text{sh}} I_K - (R_{\text{sh}} + R_s) - V_L \tag{III.9}$$

Thus, the exact predicted output current is given by comparing Eq III.8 with Eq III.9. This gives:

$$\left(\begin{array}{c} I_L = \dfrac{R_{\text{sh}}(I_{\text{ph}} + I_{\text{sd}}) - V_L}{R_{\text{sh}} + R_s} - \\ \left(\frac{n \cdot V_t}{R_s} \, \text{LambertW}\left(\frac{R_s R_{\text{sh}} I_{\text{sd}}}{n \cdot V_t (R_{\text{sh}}+R_s)} \, e^{\left(\frac{R_s}{n \cdot V_t (R_{\text{sh}}+R_s)} \left(R_{\text{sh}}(I_{\text{ph}}+I_{\text{sd}}) + \frac{R_{\text{sh}}}{R_s} V_L\right)\right)} \right) \right) \end{array} \right) \tag{III.10}$$

Eq III.10 then represents the exact solution of the nonlinear equation of the PV cell current.

III.2.2 Iterative Methods

Several iterative methods are available in the literature, some of which are highly effective for parameter estimation. The Newton-Raphson (NR) method is considered one of the best [42]; however, its accuracy and convergence can be significantly affected by an improper choice of initial conditions.

The Newton-Raphson method

The Newton-Raphson method is a robust iterative technique for solving nonlinear equations involving a single variable [43]. It is derived from the Taylor series expansion and achieves successive approximations of the equation's solution with quadratic convergence.

In the context of modeling a photovoltaic solar panel, the Newton-Raphson algorithm is a powerful tool for determining the predicted current Ipv by efficiently finding the roots of the function f (X).

It is a method based on evaluating the objective function and its derivative at a point Xn The solution is updated at each iteration using the following equation [44]:

$$X_{n+1} = X_n - \frac{f(X_n)}{f'(X_n)} \tag{III.11}$$

Where:

X_{n+1}: Represents the updated solution from the current value X_n.

$f(X_n)$: Represents the evaluation of the objective function $f(X)$ at the current value X_n.

$f'(X_n)$: Represents the evaluation of the derivative of the objective function $f(X)$ at the solution point X_n.

The application of the Newton-Raphson method to solve the following nonlinear equation:

$$f(I_L) = I_{\text{ph}} - I_L - I_{\text{sd}} \left(-1 + e^{\left(\frac{V_L + R_s I_L}{n \cdot V_t}\right)} \right) - \frac{V_L + R_s I_L}{R_{\text{sh}}} = 0 \tag{III.12}$$

Applying Newton's method allows us to calculate the value of the current Iph for each iteration by:

$$I_{L(n+1)} = I_{L(n)} - \frac{I_{\text{ph}} - I_L - I_{\text{sd}} \left(-1 + \ e^{\left(\frac{V_L + R_s I_L}{n \cdot V_t}\right)} \right) - \frac{V_L + R_s I_L}{R_{\text{sh}}}}{-1 - \frac{R_s I_{\text{sd}}}{n \cdot V_t} \ e^{\left(\frac{V_L + R_s I_L}{n \cdot V_t}\right)} - \frac{R_s}{R_{\text{sh}}}} \tag{III.13}$$

III.3 Mathematical Models of Photovoltaic Cell

Solar cell models that describe the I-V characteristics typically include one or two diodes. These detailed models are presented as follows:

III.3.1 Single-Diode Model (SDM)

The single-diode model can be described using a modified Shockley diode equation. This model is widely used for solar cell modeling due to its simplicity and the use of only five parameters (I_{ph}, I_d, n, R_{sh}, R_s). Figure III.1 illustrates the single-diode model, which consists of a current source in parallel with a diode. Additionally, the module's shunt resistance regulates current losses at the junction within the cell [4].

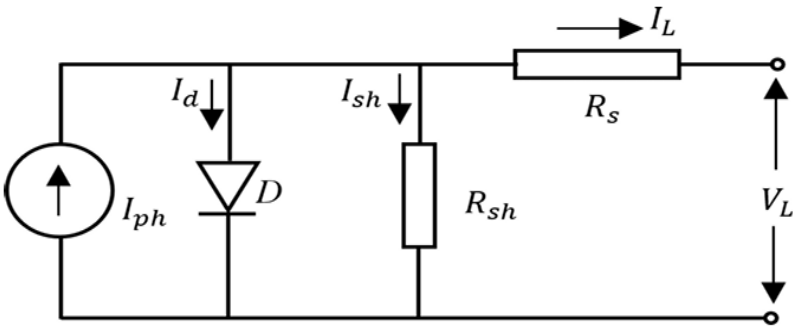


Figure III.1: Equivalent circuit of Single-Diode model solar cell [15].

$$I_L = I_{\text{ph}} - I_d - I_{\text{sh}} \tag{III.14}$$

Where I_{ph}, I_d, and I_{sh} represent the current of the independent current source, the diode current, and the current through the shunt resistance, respectively. The diode current I_d is well defined by the Shockley equation as:

$$I_d = I_{\text{sd}} \left(-1 + e^{\left(\frac{V_L + R_s I_L}{n \cdot V_t}\right)} \right) \tag{III.15}$$

Where I_{sd}, V_L, and I_L are the diode saturation current (A), the measured voltage (V), and the measured current (A), respectively. The diode ideality factor is denoted by n, and the thermal voltage is represented by V_t and is calculated as:

$$V_t = \frac{k \cdot T}{q} \tag{III.16}$$

Where k represents the Boltzmann constant and equals ($1.3806503 \times 10^{-23}$ J/K), T is the temperature measured in Kelvin ($T = 33 + 273.15$), and q is the electron charge ($1.60217646 \times 10^{-19}$ C). The shunt resistance current is formulated as:

$$I_{\text{sh}} = \frac{V_L + R_s I_L}{R_{\text{sh}}} \tag{III.17}$$

From equations III.14, III.15, III.16, and III.17, the output current of the solar cell can be calculated as [45]:

$$I_L = I_{\text{ph}} - I_{\text{sd}} \left(-1 + e^{\left(\frac{V_L + R_s I_L}{n \cdot V_t}\right)} \right) - \frac{V_L + R_s I_L}{R_{\text{sh}}} \tag{III.18}$$

In this equation, the five unknown parameters are $X = (I_{\text{ph}}, I_{\text{sd}}, R_s, R_{\text{sh}}, n)$ which have to be optimized.

III.3.2 Double-Diode model (DDM)

The single-diode model becomes significantly inaccurate at low illumination levels when describing cell behavior. This implies that the double-diode model is more accurate under solar shading. Figure III.2 shows the double-diode model, where an additional diode is added in parallel with the current source. This additional diode allows the model to achieve higher accuracy than the single-diode model. However, with seven parameters ($I_{\text{ph}}, I_{d1}, I_{d2}, n_1, n_2, R_{\text{sh}}, R_{\text{s}}$) more computational effort is required.

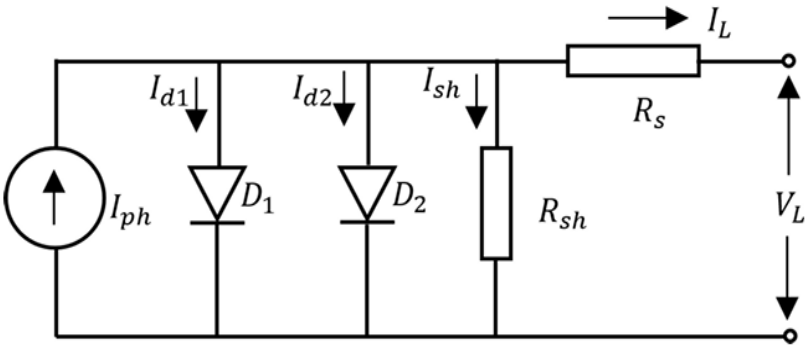


Figure III.2: Equivalent circuit of Double-Diode model solar cell [15].

$$I_L = I_{\text{ph}} - I_{d1} - I_{d2} - I_{\text{sh}} \tag{III.19}$$

$$I_{d1} = I_{sd1}\left(-1 + e^{\left(\frac{V_L + R_s I_L}{n_1 \cdot V_t}\right)}\right) \tag{III.20}$$

$$I_{d2} = I_{sd2}\left(-1 + e^{\left(\frac{V_L + R_s I_L}{n_2 \cdot V_t}\right)}\right) \tag{III.21}$$

$$I_L = I_{\text{ph}} - I_{sd1}\left(-1 + e^{\left(\frac{V_L + R_s I_L}{n_1 \cdot V_t}\right)}\right) - I_{sd2}\left(-1 + e^{\left(\frac{V_L + R_s I_L}{n_2 \cdot V_t}\right)}\right) - \frac{V_L + R_s I_L}{R_{\text{sh}}} \tag{III.22}$$

Where I_{sd1} and I_{sd2} are, respectively, the saturation currents (A) of diode 1 and diode 2. n_1 and n_2 denote the ideality factors of diode 1 and diode 2, respectively. There are seven unknown parameters in this model that must be identified:$X = (I_{\text{ph}}, I_{sd1}, I_{sd2}, R_s, R_{\text{sh}}, n_1, n_2)$.

III.4 RMSE Objective Function

To estimate the parameters of a solar cell or PV module, an objective function must first be defined and then optimized using a selected metaheuristic algorithm (MA). One of the most commonly used objective functions for this task is the Root Mean Square Error (RMSE), which aims to minimize the discrepancy between experimental and simulated I-V data, as expressed in the following equation [46]:

$$\text{RMSE} = \sqrt{\frac{1}{N_e}\sum_{i=1}^{N_e}\left(I_i^{\text{measured}} - I_i^{\text{estimated}}\right)^2} \tag{III.23}$$

Where Ne represents the number of the measured points. Iimeasured and Iiestimated represent the measured and estimated solar cell current at point i, respectively.

III.4.1 For SDM of PV Cell

The estimated current expression for the SDM using the Lambert-W function is presented as follows:

$$\begin{cases} F_{\text{obj}} = \sqrt{\dfrac{1}{N_e}\displaystyle\sum_{i=1}^{N_e}\left(I_i^{\text{measured}} - \left(\dfrac{R_{\text{sh}}(I_{\text{ph}}+I_{sd})-V_L}{R_{\text{sh}}+R_s} - \dfrac{n\cdot V_t}{R_s}W(\beta)\right)\right)^2} \\ W(\beta) = \dfrac{R_s R_{\text{sh}} I_{sd}}{n\cdot V_t(R_{\text{sh}}+R_s)} e^{\left(\frac{R_s}{n\cdot V_t(R_{\text{sh}}+R_s)}\left(R_{\text{sh}}(I_{\text{ph}}+I_{sd})+\frac{R_{\text{sh}}}{R_s}V_L\right)\right)} \end{cases} \tag{III.24}$$

The estimated current expression for the SDM using The Newton-Raphson method is presented as follows:

$$\begin{cases} F(V_L, I_L, X) = I_{\text{ph}} - I_L - I_{sd}\left(-1 + e^{\left(\frac{V_L+R_s I_L}{n\cdot V_t}\right)}\right) - \dfrac{V_L+R_s I_L}{R_{\text{sh}}} \\ X = (I_{\text{ph}}, I_{sd}, n, R_s, R_{\text{sh}}) \end{cases} \tag{III.25}$$

There are five parameters in the above two equations that need to be specified: $(I_{\text{ph}}, I_{sd}, n, R_s, R_{\text{sh}})$

III.4.2 For DDM of PV Cell

The estimated current expression for the DDM using the Lambert-W function is presented as follows [47]:

$$\begin{cases} F_{\text{obj}} = \sqrt{\dfrac{1}{N_e}\displaystyle\sum_{i=1}^{N_e}\left(I_i^{\text{measured}} - \left(\dfrac{R_{\text{sh}}(I_{\text{ph}}+I_{sd1}+I_{sd2})-V_L}{R_{\text{sh}}+R_s} - \dfrac{n_1\cdot V_t}{R_s}W(\beta_1) - \dfrac{n_2\cdot V_t}{R_s}W(\beta_2)\right)\right)^2} \\ W(\beta_i) = \dfrac{R_s R_{\text{sh}} I_{sdi}}{n_i\cdot V_t(R_{\text{sh}}+R_s)} e^{\left(\frac{R_s}{n_i\cdot V_t(R_{\text{sh}}+R_s)}\left(R_{\text{sh}}(I_{\text{ph}}+I_{sdi})+\frac{R_{\text{sh}}}{R_s}V_L\right)\right)}, \quad i=1,2 \end{cases} \tag{III.26}$$

The estimated current expression for the DDM using The Newton-Raphson method is presented as follows:

$$\begin{cases} F(V_L, I_L, X) = I_{\text{ph}} - I_L - I_{sd1}\left(-1 + e^{\left(\frac{V_L + R_s I_L}{n_1 \cdot V_t}\right)}\right) - I_{sd2}\left(-1 + e^{\left(\frac{V_L + R_s I_L}{n_2 \cdot V_t}\right)}\right) - \dfrac{V_L + R_s I_L}{R_{\text{sh}}} \\ X = (I_{\text{ph}}, I_{sd1}, I_{sd2}, n_1, n_2, R_s, R_{\text{sh}}) \end{cases} \tag{III.27}$$

There are seven parameters in the above two equations that need to be specified: ($I_{\text{ph}},\ I_{sd1},\ I_{sd2},\ n_1,\ n_2,\ R_s,\ R_{\text{sh}}$)

III.5 Results and Discussion

This section presents and analyzes the simulation results obtained using MATLAB R2024b. Four metaheuristic algorithms: the Mountain Gazelle Optimizer (MGO), Red-tailed Hawk Algorithm (RTH), Dang Beetle Optimizer (DBO), and Arctic Puffin Optimization (APO) are implemented to extract the electrical parameters of single-diode (SDM) and double-diode (DDM) photovoltaic models. The study focuses specifically on the RTC France silicon solar cell. Parameter estimation is performed using both the Newton-Raphson method and the Lambert-W function. The evaluation includes statistical metrics such as the best (minimum), mean)median), maximum, and standard deviation of the Root Mean Square Error (RMSE), computed over 1000 independent runs. The results highlight the robustness, accuracy, and convergence efficiency of the proposed metaheuristic methods in solar PV modeling.

III.5.1 RTC France Silicon Solar Cell Identification

Tableau III.1: Upper and lower bound of the SDM, DDM parameters of the RTC FRANCE solar cell.

Parameters	Lower bound	Upper bound
SDM		
I_{ph} (A)	0	1
I_{sd} (μA)	0	1
R_s (Ω)	0	0.5
R_{sh} (Ω)	0	100
n	1	2
DDM		
I_{ph} (A)	0	1
I_{sd1}, I_{sd2} (μA)	0	1
R_s (Ω)	0	0.5
R_{sh} (Ω)	0	100
n_1, n_2	1	2

The proposed optimization techniques were used to determine the parameters of the commercial silicon solar cell, R.T.C. France.

The experimental data were obtained from the system subjected to irradiation of 1000 W/m^2 at 33°C [48].

The following results present the estimation of five and seven parameters, along with the RMSE values for both the SDM and DDM models, obtained using various optimization algorithms such as MGO, RTH, DBO, APO, and others. Two methods were employed to achieve these results: the Newton-Raphson method and the Lambert-W function approach.

III.5.2 Results of Lambert-W function

III.5.2.1 Results of SDM

Table III.2 shows the model coefficients for single-diodes estimated using the MGO, RTH, DBO, and APO algorithms. The Lambert-W function was used to compute the

optimal root mean square error (RMSE). Among these methods, the RTH and APO algorithms achieved the best performance, both reaching the lowest RMSE value of **7.7301 e-04**, as reported in Table III.2.

The algorithms are ranked based on their minimum RMSE values in the following order: RTH, APO, DBO, and MGO. The I-V and P-V characteristics of the tested SDM model are derived from the results obtained using the MGO, RTH, DBO, and APO algorithms, as shown in Table III.2. These results highlight that the RTH algorithm delivers superior performance and higher accuracy in extracting the decision variables for the SDM model.

Figures III.3, III.4, III.5, and III.6 present the measured and estimated data results for the single-diode model.

Tableau III.2: Optimal parameter values for the SDM model of the RTC France silicon solar cell using Lambert-W function.

Algorithm	I_{ph} (A)	I_{sd} (μA)	R_s (Ω)	R_{sh} (Ω)	n	RMSE
MGO	0.7610	0.1891	0.0387	44.3622	1.1954	7.7425 e-04
RTH	**0.7608**	**0.3107**	**0.0365**	**52.8898**	**1.2154**	**7.7301 e-04**
DBO	0.7606	1	0.0311	100	1.2667	7.7349 e-04
APO	**0.7608**	**0.3107**	**0.0365**	**52.8898**	**1.2154**	**7.7301 e-04**

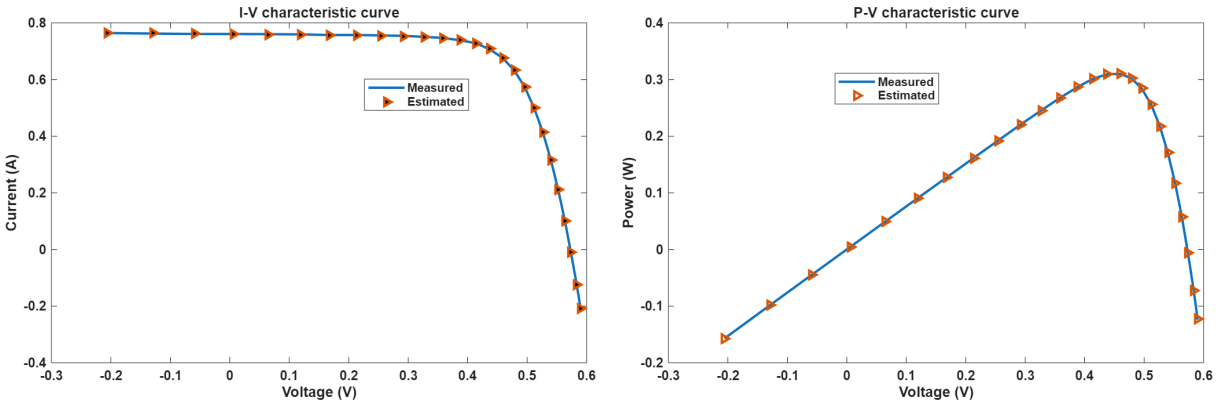


Figure III.3: The measured data and estimated data obtained by MGO of single-diode model using Lambert-W function.

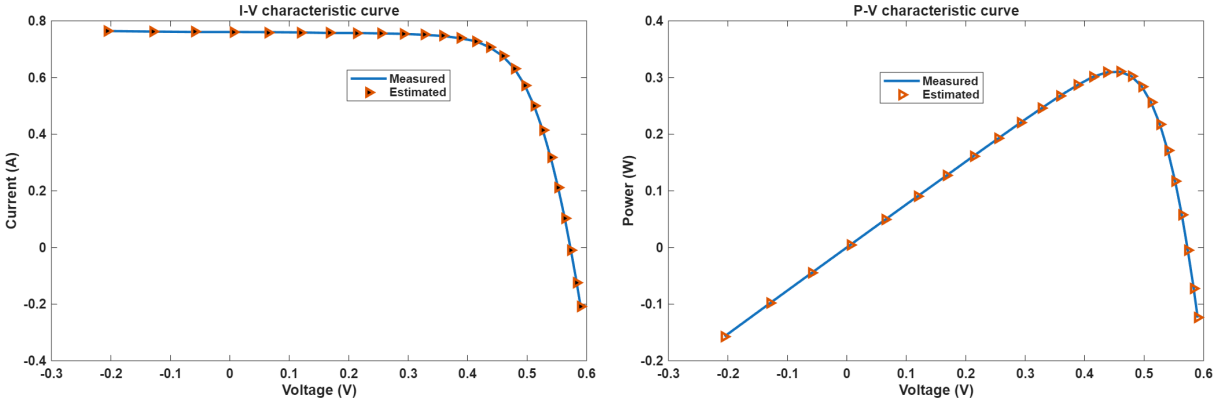


Figure III.4: The measured data and estimated data obtained by RTH of single-diode model using Lambert-W function.

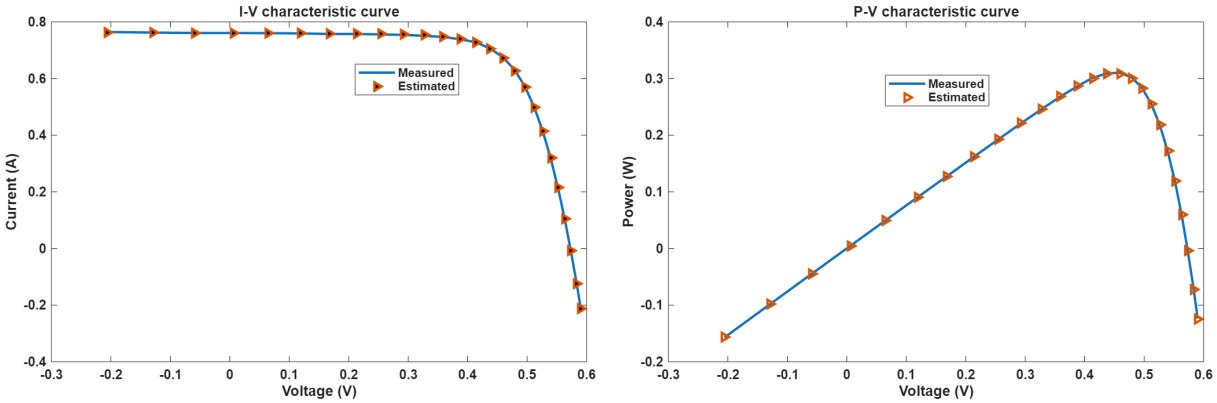


Figure III.5: The measured data and estimated data obtained by DBO of single-diode model using Lambert-W function.

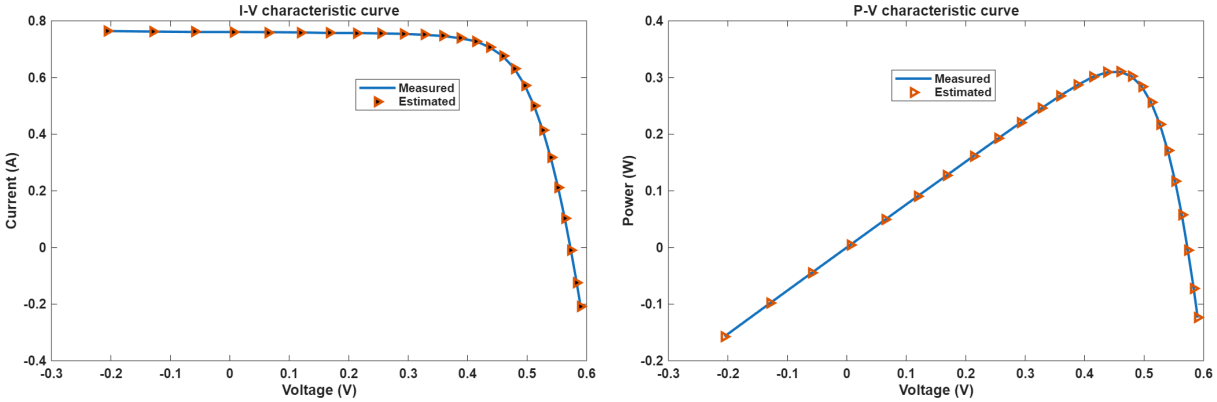


Figure III.6: The measured data and estimated data obtained by APO of single-diode model using Lambert-W function.

III.5.2.2 Results of DDM

Table III.3 presents the model coefficients of the double-diode model cell estimated using the MGO, RTH, DBO, and APO algorithms. The Lambert-W function was employed to determine the optimal root mean square error (RMSE). Among these methods, the RTH and APO algorithms achieved the lowest RMSE value of **7.5840 e-04**, as indicated in Table III.3.

Figures III.7, III.8, III.9, and III.10 present the measured and estimated data results for the double-diode model.

Tableau III.3: Optimal parameter values for the DDM model of the RTC France silicon solar cell using Lambert-W function.

Algorithm	I_{ph} (A)	I_{sd1} (μA)	I_{sd2} (μA)	R_s (Ω)	R_{sh} (Ω)	n_1	n_2	RMSE
MGO	0.7609	0.1553	1.6860 e-04	0.0457	51.6981	1.4285	1.7537	7.7650 e-04
RTH	**0.7608**	**0.2375**	**1.2816 e-04**	**0.0393**	**52.4832**	**1.4567**	**1.9709**	**7.5840 e-04**
DBO	0.7630	1	1	0.0332	100	2	1.7371	7.7024 e-04
APO	**0.7608**	**0.2158**	**0.0218**	**0.0393**	**52.4832**	**1.4567**	**1.9709**	**7.5840 e-04**

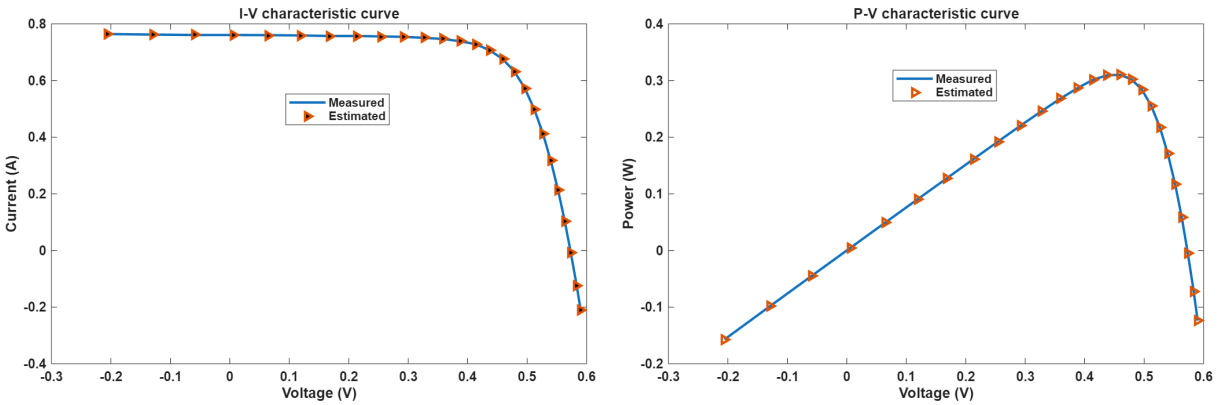


Figure III.7: The measured data and estimated data obtained by MGO of double-diode model using Lambert-W function.

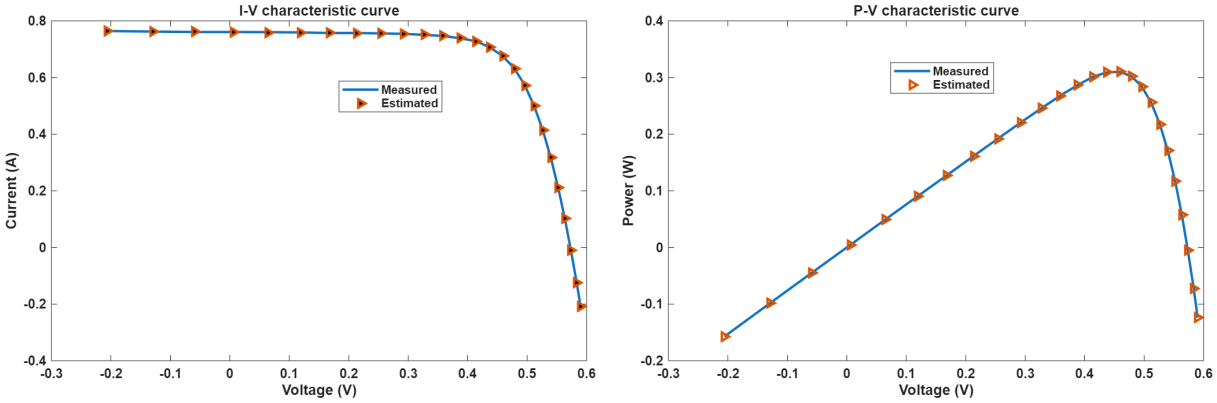


Figure III.8: The measured data and estimated data obtained by RTH of double-diode model using Lambert-W function.

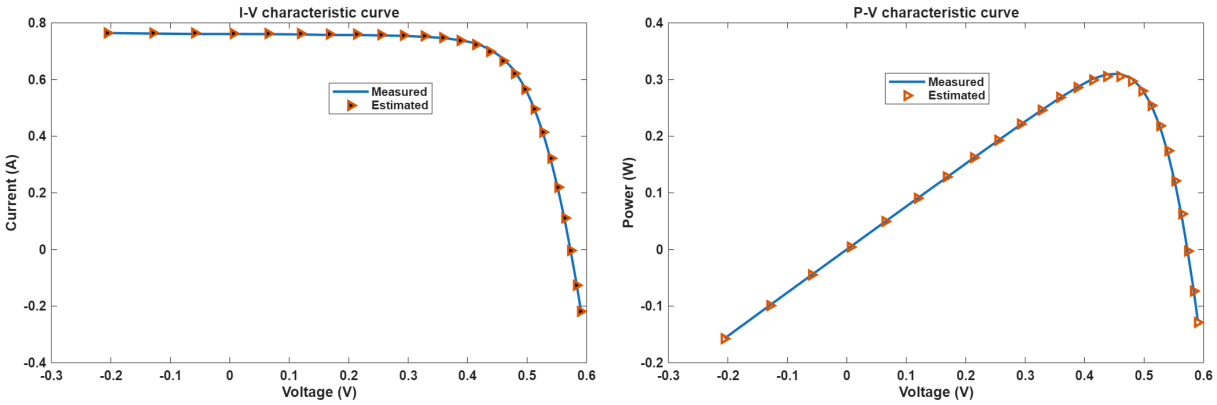


Figure III.9: The measured data and estimated data obtained by DBO of double-diode model using Lambert-W function.

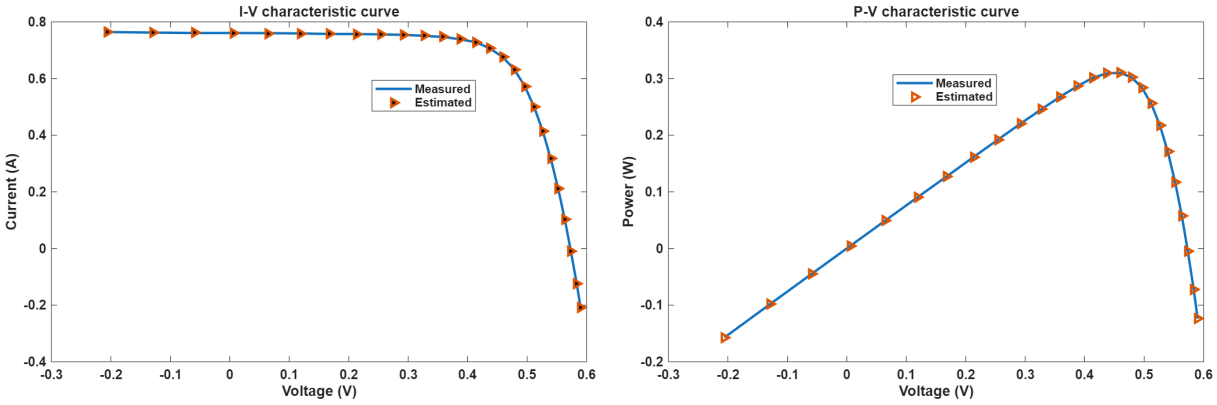


Figure III.10: The measured data and estimated data obtained by APO of double-diode model using Lambert-W function.

III.5.3 Results of Newton-Raphson method

III.5.3.1 Results of SDM

Table III.4 presents the model coefficients of the single-diode model cell, estimated using the MGO, RTH, DBO, and APO algorithms. The Newton-Raphson method was applied to obtain the optimal root mean square error (RMSE). Among these algorithms, RTH and APO achieved the lowest RMSE value of **7.7299 e-04**, as indicated in Table III.4.

The algorithms are ranked based on their minimum RMSE values in the following order: RTH, APO, DBO, and MGO. The I-V and P-V characteristics of the tested SDM model are derived from the results obtained using the MGO, RTH, DBO, and APO algorithms, as shown in Table III.4. These results highlight that the RTH algorithm delivers superior performance and higher accuracy in extracting the decision variables for the SDM model.

Figures III.11, III.12, III.13, and III.14 present the measured and estimated data results for the single-diode model.

Tableau III.4: Optimal parameter values for the SDM model of the RTC France silicon solar cell using Newton-Raphson method.

Algorithm	I_{ph} (A)	I_{sd} (μA)	R_s (Ω)	R_{sh} (Ω)	n_1	RMSE
MGO	0.7607	0.4251	0.0352	60.9185	1.5094	8.1686 e-04
RTH	**0.7608**	**0.3107**	**0.0365**	**52.8899**	**1.4773**	**7.7299 e-04**
DBO	0.7606	0.3687	0.0358	59.0940	1.4946	7.7649 e-04
APO	**0.7608**	**0.3107**	**0.0365**	**52.8899**	**1.4773**	**7.7299 e-04**

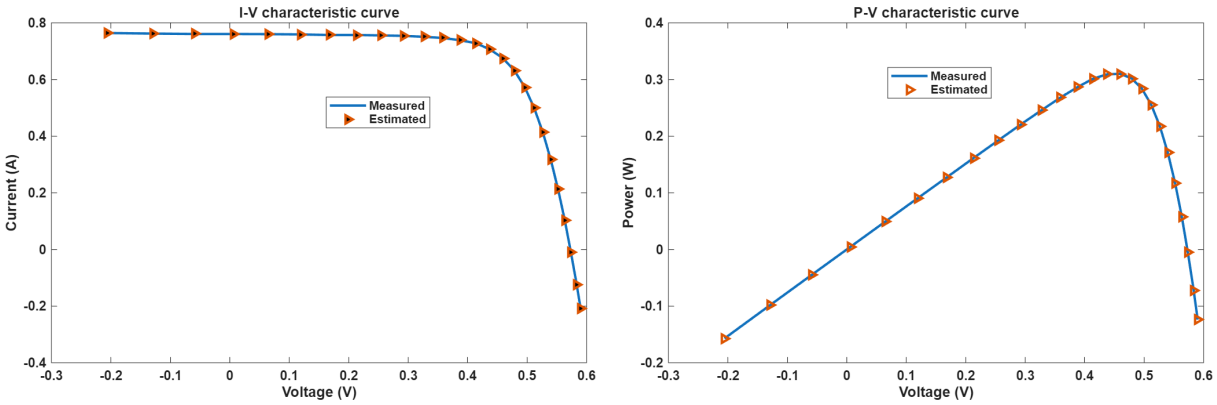


Figure III.11: The measured data and estimated data obtained by MGO of single-diode model using Newton-Raphson method.

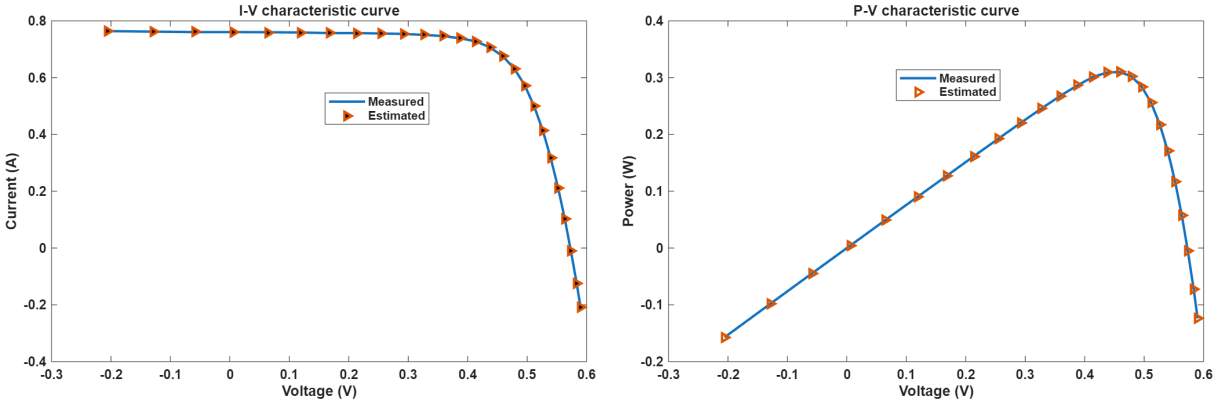


Figure III.12: The measured data and estimated data obtained by RTH of single-diode model using Newton-Raphson method .

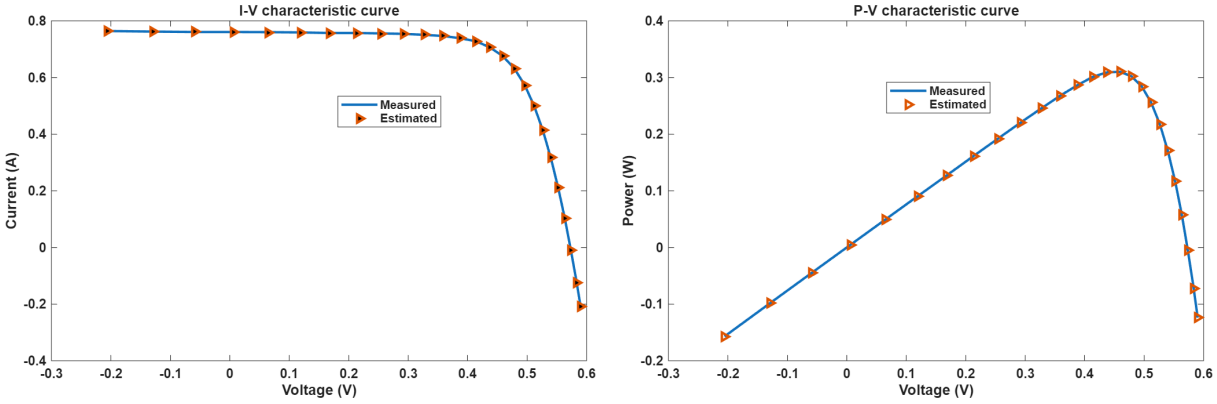


Figure III.13: The measured data and estimated data obtained by DBO of single-diode model using Newton-Raphson method.

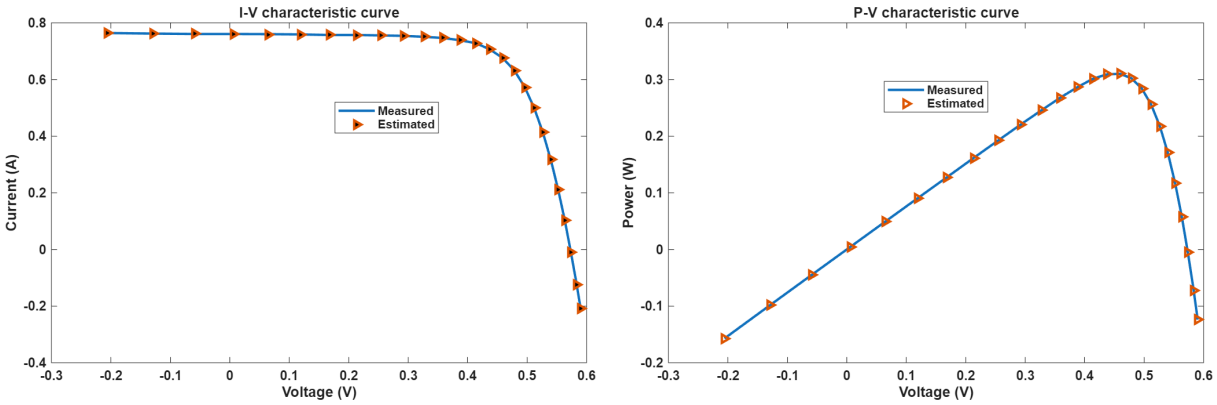


Figure III.14: The measured data and estimated data obtained by APO of single-diode model using Newton-Raphson method.

III.5.3.2 Results of DDM

Table III.5 presents the model coefficients for double-diodes estimated using the MGO, RTH, DBO, and APO algorithms. The Newton-Raphson method was applied to obtain the optimal root mean square error (RMSE). Among these algorithms, RTH achieved the lowest RMSE value of **7.4194 e-04**, as indicated in Table III.5.

Figures III.15, III.16, III.17, and III.18 present the measured and estimated data results for the double-diode model.

Tableau III.5: Optimal parameter values for the DDM model of the RTC France silicon solar cell using Newton-Raphson method.

Algorithm	I_{ph} (A)	I_{sd1} (μA)	I_{sd2} (μA)	R_s (Ω)	R_{sh} (Ω)	n_1	n_2	RMSE
MGO	0.7607	0.0955	0.2778	0.0364	54.7690	1.4271	1.5415	7.6934 e-04
RTH	**0.7608**	**0.0969**	**0.9999**	**0.0376**	**55.7752**	**1.3863**	**1.8358**	**7.4194 e-04**
DBO	0.7607	1	0.2518	0.0359	61.6734	2	1.4633	7.9170 e-04
APO	0.7608	0.2099	0.3691	0.0368	53.9743	1.4466	1.8130	7.5750 e-04

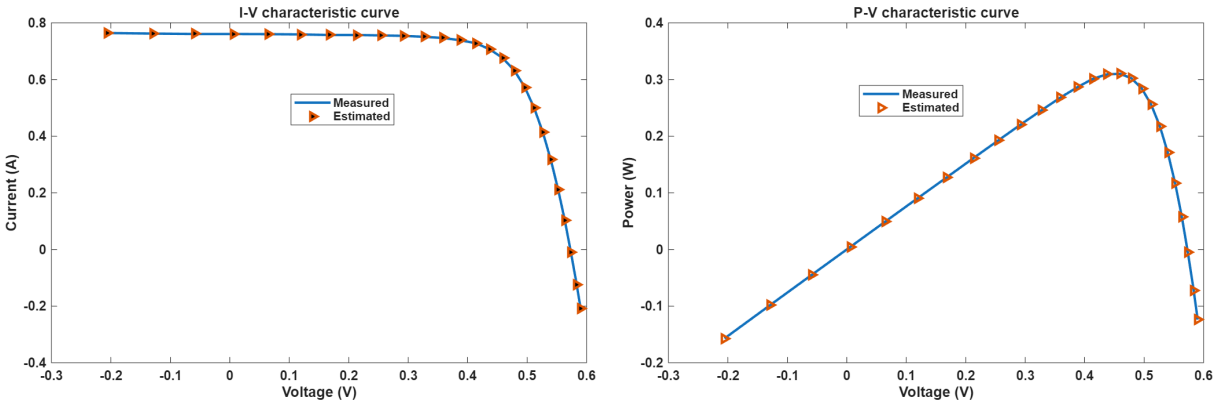


Figure III.15: The measured data and estimated data obtained by MGO of double-diode model using Newton-Raphson method.

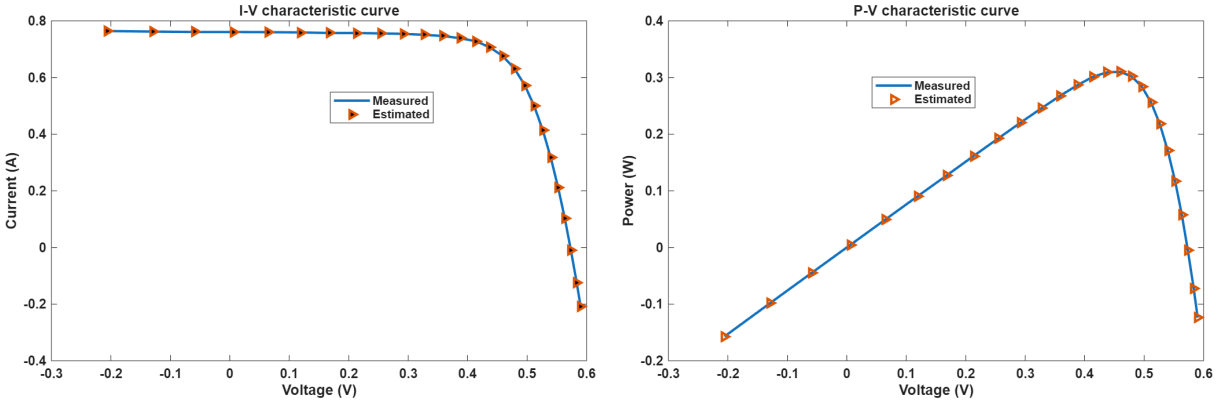


Figure III.16: The measured data and estimated data obtained by RTH of double-diode model using Newton-Raphson method.

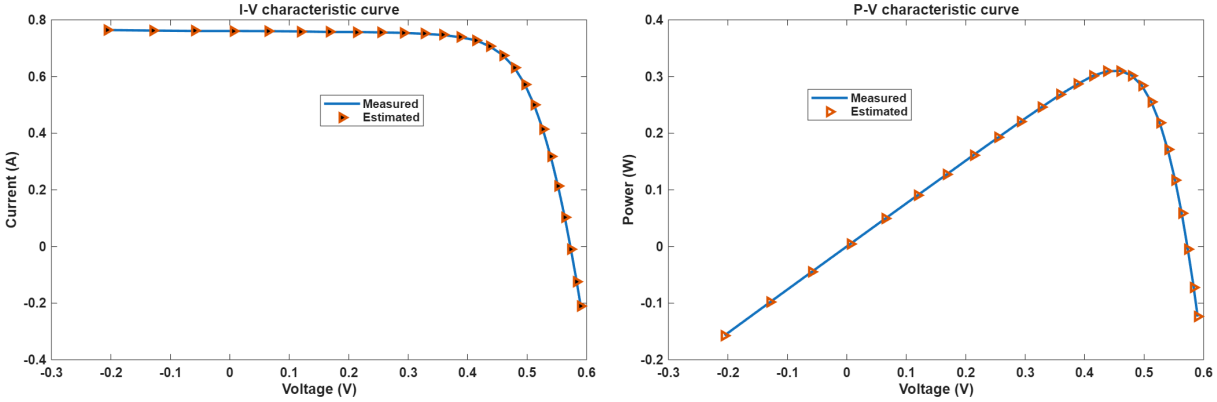


Figure III.17: The measured data and estimated data obtained by DBO of double-diode model using Newton-Raphson method.

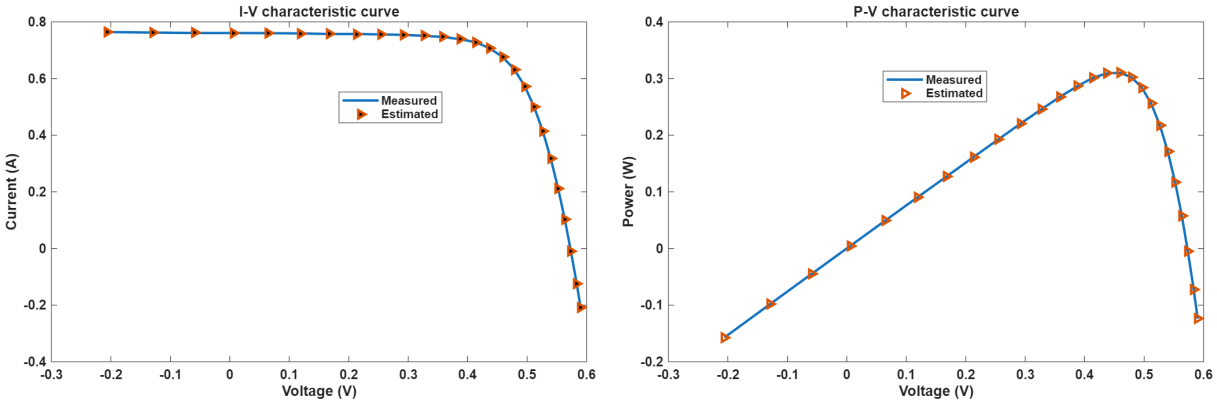


Figure III.18: The measured data and estimated data obtained by APO of double-diode model using Newton-Raphson method.

III.5.4 Statistics Analysis

III.5.4.1 The Lambert-W function

To assess the robustness and reliability of the RTH algorithm, Table III.6 and Table III.7 present the statistical results obtained using MGO, RTH, DBO, and APO for the SDM and DDM of RTC France silicon solar cells.

These results include: RMSE min, which represents the lowest value of RMSE; RMSE mean, which corresponds to the average value of RMSE; RMSE max, which is the worst value; STD, which is the standard deviation of the RMSE values; and it indicates the reliability of the algorithm.

Tableau III.6: Statistical analysis of SDM using Lambert-W function.

SDM				
Algorithm	$RMSE_{min}$	$RMSE_{mean}$	$RMSE_{max}$	STD
MGO	7.7425e-04	0.0011	0.0020	3.5229e-04
RTH	**7.7301e-04**	**7.7301e-04**	**7.7301e-04**	**1.1321e-16**
DBO	7.7349e-04	0.0013	0.0021	4.5484e-04
APO	7.7301e-04	7.7301e-04	7.7301e-04	1.4170e-17

The SDM identified through the RTH algorithm achieves the lowest RMSE value after 1000 iterations, with a standard deviation of **1.1321 e-16**.

Tableau III.7: Statistical analysis of DDM using Lambert-W function.

DDM				
Algorithm	$RMSE_{min}$	$RMSE_{mean}$	$RMSE_{max}$	STD
MGO	7.7650e-04	8.5466e-04	9.7255e-04	6.0202e-05
RTH	**7.5840e-04**	**7.6132e-04**	**7.7301e-04**	**6.1577e-06**
DBO	7.7024e-04	0.0023	0.0053	0.0018
APO	7.5840e-04	7.5901e-04	7.6413e-04	1.8002e-06

The identification of the parameters of the RTC France cell based on the DDM shows that the best results are obtained by RTH, which records an RMSE of **7.5840 e-04** and STD of **6.1577 e-06**.

III.5.4.2 Newton-Raphson method

To assess the robustness and reliability of the RTH algorithm, Table III.8 and Table III.9 present the statistical results obtained using MGO, RTH, DBO, and APO for the SDM and DDM of RTC France silicon solar cells.

Tableau III.8: Statistical analysis of SDM using Newton-Raphson method.

SDM				
Algorithm	$RMSE_{min}$	$RMSE_{mean}$	$RMSE_{max}$	STD
MGO	8.1686e-04	9.1608e-04	0.0012	1.2861e-04
RTH	**7.7299e-04**	**7.7299e-04**	**7.7299e-04**	**4.5898e-17**
DBO	7.7649e-04	0.0014	0.0021	5.3187e-04
APO	7.7299e-04	7.7299e-04	7.7299e-04	1.2186e-17

For SDM identified based on RTH, it is found that the lowest RMSE value is reached after 1000 iterations, with an STD of **4.5898 e-17**.

Tableau III.9: Statistical analysis of DDM using Newton-Raphson method.

DDM				
Algorithm	$RMSE_{min}$	$RMSE_{mean}$	$RMSE_{max}$	STD
MGO	7.6934e-04	9.1901e-04	0.0011	1.5350e-04
RTH	**7.4194e-04**	**7.4213e-04**	**7.4294e-04**	**5.2044e-06**
DBO	7.9170e-04	0.0014	0.0021	6.2985e-04
APO	7.5750e-04	7.6320e-04	7.6837e-04	3.6002e-06

For the France RTC cell based on DDM, the best results are obtained by RTH, which records an STD of **5.2044 e-06**.

III.5.5 Convergence Analysis

The graph illustrates the convergence patterns of the objective function (RMSE) for both the SDM and DDM models applied to the RTC France solar cell. It is noteworthy that the DDM model exhibited faster and more efficient convergence compared to the SDM model. During the optimization process, the Lambert-W function and the Newton-Raphson method were employed to enhance accuracy and efficiently determine the optimal roots.

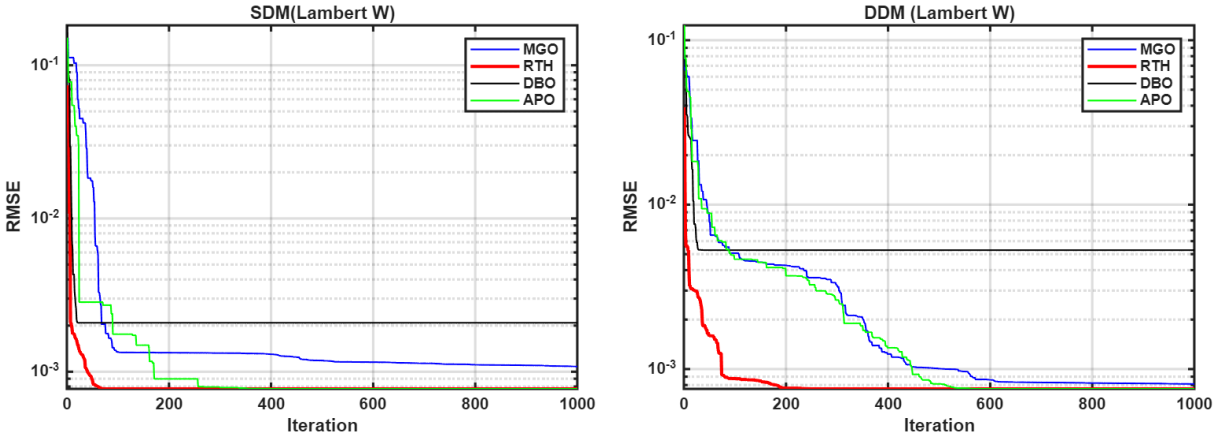


Figure III.19: Convergence curves for SDM and DDM of France silicon solar cell using Lambert-W function.

In the case of the Lambert-W function, Figure III.19 illustrates the fastest convergence speeds achieved across separate runs of the MGO, RTH, DBO, and APO algorithms. The RTH algorithm demonstrated a significant improvement in convergence for both the SDM and DDM models compared to the other approaches.

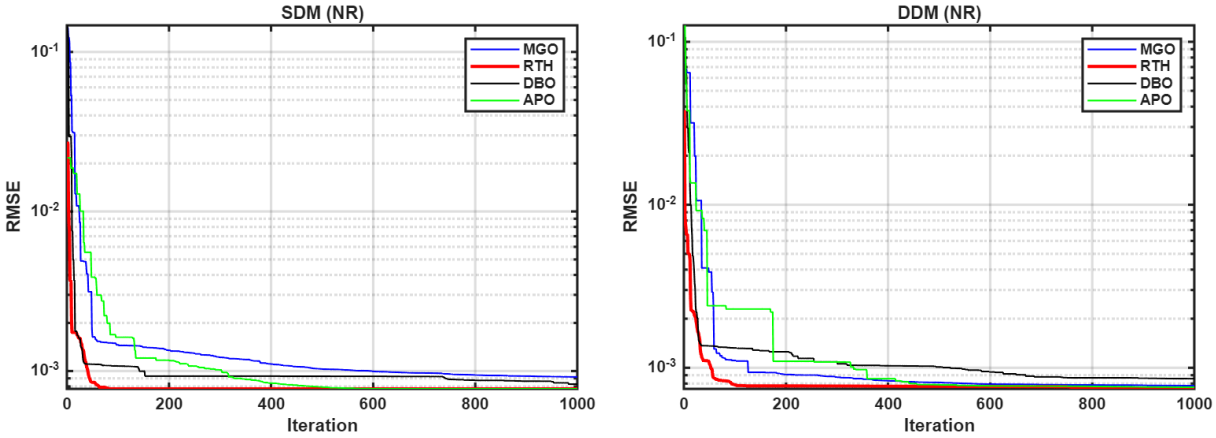


Figure III.20: Convergence curves for SDM and DDM of France silicon solar cell using Newton-Raphson method.

For the Newton-Raphson method, Figure III.20 presents the best convergence speeds observed during separate runs of the MGO, RTH, DBO, and APO algorithms. Similarly, the RTH algorithm achieved the fastest convergence for both the SDM and DDM models, outperforming the other algorithms.

Based on the decision coefficients obtained for the single- and double-diode models estimated using the MGO, RTH, DBO, and APO algorithms, both the Lambert W function and the Newton-Raphson method were applied. Their results were analyzed and compared to determine the optimal root mean square error (RMSE). Among the algo-

rithms tested, the RTH algorithm consistently achieved the lowest RMSE value using both methods. Although the results from the Newton-Raphson method were very close to those from the Lambert-W function, a key difference exists: the Lambert-W function provides a direct analytical solution, leading to faster and more stable convergence, whereas the Newton-Raphson method is iterative and can be sensitive to the initial guess, potentially requiring more computation steps to achieve convergence.

III.6 Conclusion

This study introduced the MGO, RTH, DBO, and APO algorithms as advanced phenomenological analysis techniques for solving optimization problems, particularly in estimating parameters of single- and double-diode photovoltaic (PV) models. The optimization capabilities of these algorithms were thoroughly evaluated using an explicit, non-iterative objective function based on the Lambert W function for RMSE minimization, alongside the Newton-Raphson method.

The obtained simulation results, based on benchmark silicon solar cell data from RTC France, demonstrated the outstanding performance of the RTH algorithm. RTH consistently achieved the lowest RMSE values, exhibited greater robustness and consistency across multiple runs (evidenced by lower standard deviations), and achieved faster convergence compared to the other algorithms for both SDM and DDM models. Additional comparisons using the Lambert-W function and the Newton-Raphson method confirmed the superior performance of RTH. While both methods produced similar results, the Lambert-W function enabled faster and more stable convergence due to its direct analytical formulation, unlike the Newton-Raphson method, which, being iterative, was more sensitive to initial conditions and required more computational effort.

General Conclusion

This study addressed the complex nonlinear optimization problem of parameter estimation in single- and double-diode photovoltaic (PV) cell models. To tackle this challenge, four recent nature-inspired metaheuristic algorithms were employed: the Mountain Gazelle Optimizer (MGO), Red-Tailed Hawk Algorithm (RTH), Dung Beetle Optimizer (DBO), and Arctic Puffin Optimization (APO). The parameter extraction process was guided by an explicit, non-iterative objective function based on the Lambert-W function, designed to minimize the Root Mean Square Error (RMSE). For benchmarking purposes, the classical Newton-Raphson method was also implemented.

Chapter I laid the theoretical foundation by presenting the fundamentals of photovoltaic systems, including the photovoltaic effect, the structure and types of solar cells, and the influence of environmental factors such as irradiance and temperature. It also discussed the benefits and limitations of solar energy, underscoring the importance of accurate modeling for improving PV system performance.

Chapter II introduced the selected metaheuristic algorithms, detailing their operating mechanisms and justifying their application to PV parameter estimation problems due to their ability to navigate high-dimensional and nonlinear search spaces effectively.

In **Chapter III**, simulation results using real-world experimental data from the RTC France silicon solar cell highlighted the outstanding performance of the Red-Tailed Hawk Algorithm (RTH). RTH consistently achieved the lowest RMSE values, demonstrated greater robustness (as indicated by lower standard deviations), and converged more rapidly across multiple independent runs. Its effectiveness was evident in both the single-diode model (SDM) and the double-diode model (DDM). Furthermore, the integration of the Lambert-W function significantly enhanced computational stability and efficiency, offering a clear advantage over the Newton-Raphson method, which proved more sensitive to initial values and required more iterations for convergence.

In conclusion, the findings position RTH as a highly effective and reliable optimization algorithm for PV parameter estimation. Its consistent accuracy, rapid convergence, and robustness across diverse modeling scenarios make it a strong candidate for broader applications in photovoltaic modeling, optimization, and the development of sustainable energy systems.

Looking ahead, future research could explore the application of RTH to other PV technologies, such as thin-film or perovskite solar cells, and assess its scalability to larger PV arrays or grid-integrated systems. Moreover, integrating RTH with hybrid metaheuristic frameworks may further improve its convergence behavior and accuracy. Investigating its performance under noisy or incomplete experimental data could also enhance its practical applicability for real-time monitoring and long-term performance evaluation in real-world PV deployments.

Bibliography

[1] T.-Z. Ang, M. Salem, M. Kamarol, H. S. Das, M. Alhuyi Nazari, and N. Prabaharan. A comprehensive study of renewable energy sources: Classifications, challenges and suggestions. *Energy Strategy Reviews*, 43:100939, 2022.

[2] M. M. Hasan, S. Hossain, M. Mofijur, Z. Kabir, I. A. Badruddin, T. M. Y. Khan, and E. Jassim. Harnessing solar power: A review of photovoltaic innovations, solar thermal systems, and the dawn of energy storage solutions. *Energies*, 16(18):6456, 2023.

[3] A. O. Ali, A. T. Elgohr, M. H. El-Mahdy, H. M. Zohir, A. Z. Emam, M. G. Mostafa, M. Al-Razgan, H. M. Kasem, and M. S. Elhadidy. Advancements in photovoltaic technology: A comprehensive review of recent advances and future prospects. *Energy Conversion and Management: X*, 26:100952, 2025.

[4] A. Malki, A. A. Mohamed, Y. I. Rashwan, R. A. El-Sehiemy, and M. A. Elhosseini. Parameter identification of photovoltaic cell model using modified elephant herding optimization-based algorithms. *Applied Sciences*, 11(24):11929, 2021.

[5] N. M. Abd, A. Shannan, N. Z. Yahaya, and B. S. M. S. Singh. Single-diode model and two-diode model of pv modules: A comparison. In *IEEE International Conference on Control System, Computing and Engineering (ICCSCE)*, Penang, Malaysia, November 2014.

[6] S. M. Almufti, A. Ahmad Shaban, R. Ismael Ali, and J. A. Dela Fuente. Overview of metaheuristic algorithms. *Polaris Global Journal of Scholarly Research and Trends*, 2(2):10–32, 2023.

[7] M. R. S. Shaikh, S. B. Waghmare, S. S. Labade, P. V. Fuke, and A. Tekale. A review paper on electricity generation from solar energy. *International Journal for Research in Applied Science & Engineering Technology (IJRASET)*, 5(IX):1884–1887, 2017.

[8] M. A. Halabi, A. Al-Qattana, and A. Al-Otaibi. Application of solar energy in the oil industry—current status and future prospects. *Renewable and Sustainable Energy Reviews*, 43:296–314, 2015.

[9] M. Aghaei, A. Nedaei, A. Eskandari, and J. Milimonfared. Introductory chapter: Solar photovoltaic energy. In *Solar Energy Advancements and Applications*, pages 1–10. 2022.

[10] B. K. Madhu. Dynamic analysis of grid connected hybrid system of pv panel and wind turbines for a light commercial building. Master's thesis, University of Tennessee at Chattanooga, 2010.

[11] S. Al-Ali, A. G. Olabi, and M. Mahmoud. A review of solar photovoltaic technologies: Developments, challenges, and future perspectives. *Energy Conversion and Management: X*, 2025.

[12] C. Chalkias, A. Faka, and K. Kalogeropoulos. Assessment of the direct sunlight on rural road network through solar radiation analysis using gis. *Open Journal of Applied Sciences*, 3(2):224–231, 2013.

[13] M. Alayat and I. Boucetta. Maximisation de la production d'un système photovoltaïque à base de mppt soumis à des éclairements différents. Mémoire de master, Université Badji Mokhtar - Annaba, 2017.

[14] N. Benbaha. *Commande robuste : Application à la machine à courant alternatif alimentée par un générateur photovoltaïque.* Thèse de doctorat en sciences, Université Batna 2 – Mostefa Ben Boulaïd, 2022.

[15] N. Rai, A. Abbadi, F. Hamidia, N. Douifi, B. Abdul Samad, and K. Yahya. Biogeography-based teaching learning-based optimization algorithm for identifying one-diode, two-diode and three-diode models of photovoltaic cell and module. *Mathematics*, 11(8):1861, 2023.

[16] G. D. Price. *Renewable power and energy: Photovoltaic systems*, volume 1. 2018.

[17] D. Chiras. *Solar electricity basics – Revised and updated 2nd edition: Powering your home or office with solar energy.* 2019.

[18] S. Y. Medani and Y. Bachene. Mppt-remora control of a pumping photovoltaic system. Master's dissertation, Dr Yahya Fares University, Medea, 2024.

[19] W. Ding. Comparison between perovskite and silicon for photovoltaic cell applications and future industrial prospects, 2024.

[20] Y. Doumbia. *Elaboration and characterisation of organic-inorganic hybrid perovskite thin films for photovoltaic solar cells.* Phd thesis, Universidad Polytechnic Valencia, Spain, 2024.

[21] H. Ibrahim and N. Anani. Variations of pv module parameters with irradiance and temperature. In *Proceedings of the 9th International Conference on Sustainability in Energy and Buildings (SEB-17)*, volume 134 of *Energy Procedia*, pages 276–285, 2017.

[22] G. Lyu, F. A. Siddiqui, M. M. Aman, S. H. H. Shah, A. Ali, A. M. Soomar, and S. Shaikh. Improved maximum power point tracking algorithms by using numerical analysis techniques for photovoltaic systems. *Renewable and Sustainable Energy Reviews*, 21:101740, 2024.

[23] A. El-Fergany. Parameters identification of pv model using improved slime mould optimizer and lambert w-function. *Energy Reports*, 7(7):875–887, 2021.

[24] R. Mahto and R. John. Modeling of photovoltaic module. In *Solar Cells - Theory, Materials, and Recent Advances*, pages 1–10. 2021.

[25] V. Tomar, M. Bansal, and P. Singh. Metaheuristic algorithms for optimization: A brief review. *Engineering Proceedings*, 59(1):1–6, 2024.

[26] D. Hamdi and Dj. Korichi. A contrastive analysis between the performance of four metaheuristic algorithms for parameter estimation in photovoltaic models. Master's thesis, Kasdi Merbah University Ouargla, 2024.

[27] N. Khodadadi, E.-S. M. El-Kenawy, F. De Caso, A. H. Alharbi, D. S. Khafaga, and A. Nanni. The mountain gazelle optimizer for truss structures optimization. *Applied Computing and Intelligence*, 3(2):116–144, 2023.

[28] B. Abdollahzadeh, F. S. Gharehchopogh, N. Khodadadi, and S. Mirjalili. Mountain gazelle optimizer: A new nature-inspired metaheuristic algorithm for global optimization problems. *Advances in Engineering Software*, 174:103282, 2022.

[29] S. Ferhatia, A. Houari, H. Rezk, A. Djerioui, M. Machmoum, S. Motahhir, and M. Ait-Ahmed. Red-tailed hawk algorithm for numerical optimization and real-world problems. *Scientific Reports*, 13(12950):1–17, 2023.

[30] J. Xue and B. Shen. Dung beetle optimizer: A new meta-heuristic algorithm for global optimization. *The Journal of Supercomputing*, 79(7):7305–7336, 2022.

[31] W. Cao, Z. Liu, H. Song, G. Li, and B. Quan. Dung beetle optimized fuzzy pid algorithm applied in four-bar target temperature control system. *Applied Sciences*, 14(10):1–20, 2024.

[32] C. Mai, L. Zhang, X. Chao, X. Hu, X. Wei, and J. Li. A novel mppt technology based on dung beetle optimization algorithm for pv systems under complex partial shade conditions. *Scientific Reports*, 13:1–15, 2023.

[33] L. Wang, W. Tian, D.-M. Xu, and H.-F. Zang. Arctic puffin optimization: A bio-inspired metaheuristic algorithm for solving engineering design optimization. *Advances in Engineering Software*, 195:1–12, 2024.

[34] L. Sun and B. Wang. Arctic puffin optimization algorithm based on multi-strategy blending. *Journal of Computer and Communications*, 12(12):1–15, 2024.

[35] P. Sharma and S. Raju. Metaheuristic optimization algorithms: A comprehensive overview and classification of benchmark test functions. *Soft Computing*, 27:3123–3186, 2023.

[36] Y.-L. Wang, Y.-Z. Sun, L.-L. Peng, and Y. Xu. Parameter extraction for photovoltaic module based on lambert w function. *Acta Physica Sinica*, 61(24):248402, 2012.

[37] L. Reis, R. J. Camacho, and D. Novacki. The newton raphson method in the extraction of parameters of pv modules. *Renewable Energy and Power Quality Journal*, 15(1):634–639, 2017.

[38] J. J. Soon and K.-S. Low. Photovoltaic model identification using particle swarm optimization with inverse barrier constraint. *IEEE Transactions on Power Electronics*, 27(9):3975–3983, 2012.

[39] A. Benkassis. Étude et modélisation d'un panneau photovoltaïque. Master's thesis, Université 8 Mai 1945 – Guelma, 2024.

[40] B. Gélis, V. Creuze, C. Glaize, F. Lecat, and V. Thomas. Travaux pratiques de caractérisation de panneaux photovoltaïques. In *CETSIS: 10e Colloque sur l'enseignement des technologies et des sciences de l'information et des systèmes*, pages 001–006, 2013.

[41] E. Batzelis, G. Anagnostou, C. Chakraborty, and B. C. Pal. Computation of the lambert w function in photovoltaic modeling. In *2019 IEEE Milan Power Tech*, pages 1–6, 2019.

[42] A. S. Tummala. Parameter estimation of solar pv models with quantum-based avian navigation optimizer and newton–raphson method. *Journal of Computational Electronics*, 21(6), 2022.

[43] J. G. Triana Laverde. On the newton-raphson method and its modifications. *Revista Colombian de Física*, 14(2):75–80, 2023.

[44] A. Zein. A new family of optimal fourth-order iterative methods for solving nonlinear equations with applications. *Journal of Applied Mathematics*, pages Article ID 9955247, 22 pages, 2024.

[45] A. Rezaee Jordehi. Parameter estimation of solar photovoltaic (pv) cells: A review. *Renewable and Sustainable Energy Reviews*, 61:354–371, 2016.

[46] Z. Abdennebi and A. Ghebghoub. Estimation of photovoltaic system parameters via metaheuristic algorithms. Master's thesis, University Yahya Fares of Medea, 2024.

[47] A. Abbadi, F. Hamidia, A. Morsli, M. R. Skender, and N. Douifi. Improvement of double diode model of solar cells using mountain gazelle optimization algorithm and based on lambert's w function. In *Proceedings of the 8th International Conference on Artificial Intelligence in Renewable Energetic Systems (IC-AIRES 2024)*, Medea, Algeria, 2024.

[48] A. Abbadi, F. Hamidia, M. R. Skender, K. Derbali, N. Douifi, and M. R. Chandarli. Accurate three-diode model estimation of solar cells using starfish optimization algorithm. In *Third Algerian Symposium on Renewable Energy & Materials (ASREM'25)*, Medea, Algeria, 2025.

Appendix A

Experimental Data and Measurements

Tableau A.1: Measured Current and Voltage Values.

$I_{\mathbf{measured}}$ **(A)**	$V_{\mathbf{measured}}$ **(V)**
0.764	-0.2057
0.762	-0.1291
0.7605	-0.0588
0.7605	0.0057
0.76	0.0646
0.759	0.1185
0.757	0.1678
0.757	0.2132
0.7555	0.2545
0.754	0.2924
0.7505	0.3269
0.7465	0.3585
0.7385	0.3873
0.728	0.4137
0.7065	0.4373
0.6755	0.459
0.632	0.4784
0.573	0.496
0.499	0.5119
0.413	0.5265
0.3165	0.5398
0.212	0.5521
0.1035	0.5633
-0.01	0.5736
-0.123	0.5833
-0.21	0.59